

## Structural and ethylene oligomerization studies of chelating (imino)phenol

### Fe(II), Co(II) and Ni(II) complexes: Experimental and theoretical approach

Makhosonke Ngcobo,<sup>a</sup> Holliness Nose,<sup>b</sup> Arumugam Jayamani,<sup>a\*</sup> Stephen O. Ojwach<sup>a\*</sup>

<sup>a</sup>*School of Chemistry and Physics, University of KwaZulu-Natal, Private Bag X01, Scottsville, Pietermaritzburg 3209, South Africa.*

<sup>b</sup>*School of Chemistry and Material Science, Technical University of Kenya, Haile Selasie Avenue, P.O. Box 52428-00200, Nairobi, Kenya.*

### Supplementary Information

S I. No.	Contents	Page No.
1	Syntheses of Schiff base ligands and their spectroscopic data	3
2	<b>Figures S1-S6:</b> <sup>1</sup> H NMR and <sup>13</sup> C { <sup>1</sup> H} NMR spectra of the Schiff base ligands (L1H-L3H).	4
3	<b>Figures S7-S18:</b> FTIR spectra of the ligands and complexes	7
4	<b>Figures S19-S30:</b> Mass spectrometric analyses of the ligands and complexes.	14
5	<b>Figure S31:</b> UV-Vis studies of the complexes.	25
7	<b>Figure S32:</b> GC-FID spectrum obtained using MMAO activator.	26
8	<b>Figure S33:</b> GC-FID spectrum observed in toluene solvent.	27
9	<b>Figure S34:</b> GC-FID spectrum obtained in chlorobenzene using <i>n</i> -heptane internal standard.	28
11	<b>Figure S35:</b> Effect of temperature on product distribution	28
12	<b>Figure S36:</b> B3LYP optimized geometries of the metal complexes using Lanl2dz basis set for metal cation and 6-311G(dp) basis set for the remaining atoms.	29

11	<b>Figure S37:</b> Dependence of catalytic activities in ethylene oligomerization of the metal complexes on their frontiers orbitals.	30
12	<b>Figure S38:</b> Dependence of catalytic activities in ethylene oligomerization on the global softness and chemical hardness of the metal complexes.	30
13	<b>Figure S39:</b> Dependence of catalytic activities on chemical and ionization potentials of the metal complexes	31
14	<b>Table S1:</b> X-ray crystallographic data and structure refinement for the <b>Fe3a</b> and <b>Ni3</b> complexes.	32
15	<b>Table S2:</b> Theoretical and experimental electronic transitions, oscillator strengths and assignments for metal compounds.	33
16	<b>Table S3:</b> DFT HOMO and LUMO frontier molecular orbitals of the (imino)phenol Fe(II), Co(II) and Ni(II) complexes.	34
17	<b>Table S4:</b> Optimization of the reaction conditions in ethylene oligomerization reactions using <b>Ni1</b> /EtAlCl <sub>2</sub> system.	37
18	<b>Scheme S1:</b> Proposed mechanism of ethylene oligomerization and isomerization reactions catalysed by the metal complexes	38

## **1. Synthesis of Schiff base ligands**

### ***1.1. 2,4-dibromo-6-((pyridin-2-ylimino)methyl)phenol (L1H)***

To the ethanolic (10 mL) solution of 2-aminopyridine (0.19 g, 2 mmol), 3,5-dibromosalicylaldehyde (0.56 g, 2 mmol) in ethanol (10 mL) was added dropwise and stirred at room temperature for 24 h. The orange powder formed was filtered, washed with ethanol, and dried to obtain pale orange powder. Yield: 0.61 g (81%). <sup>1</sup>H NMR (400 MHz,

CDCl<sub>3</sub>, δ ppm): 9.42 (s, 1H, imine HC=N-), 8.55 (d, 1H, <sup>3</sup>J<sub>HH</sub> = 9.2 Hz, Py-CH=N), 7.84 (t, 1H, <sup>3</sup>J<sub>HH</sub> = 7.2 Hz, Py-H), 7.80 (s, 1H, Ph-H), 7.60 (s, 1H, Ph-H), 7.34 (t, 1H, <sup>3</sup>J<sub>HH</sub> = 7.2 Hz, Py-H), 7.31 (d, 1H, <sup>3</sup>J<sub>HH</sub> = 9.2 Hz, Py-H); <sup>13</sup>C NMR (CDCl<sub>3</sub>): δ/ppm: 110.22, 113.57, 120.60, 123.45, 124.46, 134.51, 138.79, 138.88, 149.19, 153.84, 159.76, 162.28; IR ν<sub>max</sub>/ cm<sup>-1</sup>: 3058 (ν<sub>OH</sub>), 1606 (ν<sub>C=N</sub>). ESI-MS: m/z (%) 354.87 (100%) [M-H]<sup>+</sup>.

### 1.2. 2,4-dibromo-6-(((4-methylpyridin-2-yl)imino)methyl)phenol (**L2H**)

Ligand **L2H** was synthesized following the same procedure adopted for **L1H** using 2-amino-4-methylpyridine (0.21 g, 2 mmol) and 3,5-dibromosalicylaldehyde (0.56 g, 2 mmol) to give orange powder. Yield: 0.65 g (82%). <sup>1</sup>H NMR (400 MHz, CDCl<sub>3</sub>, δ ppm): 9.39 (s, 1H, imine HC=N-), 8.39 (d, 1H, <sup>3</sup>J<sub>HH</sub> = 9.2 Hz, Py-CH=N), 7.80 (s, 1H, Ph-H), 7.59 (s, 1H, Ph-H), 7.18 (s, 1H, Py-H), 7.12 (d, 1H, <sup>3</sup>J<sub>HH</sub> = 9.2 Hz, Py-H), 2.45 (s, 3H, Py-CH<sub>3</sub>); <sup>13</sup>C {<sup>1</sup>H} NMR (CDCl<sub>3</sub>): δ/ppm: 20.99, 110.87, 112.57, 120.38, 121.29, 124.46, 134.43, 138.79, 148.81, 150.32, 155.84, 158.76, 162.08; IR ν<sub>max</sub>/ cm<sup>-1</sup>: 3069 (ν<sub>OH</sub>), 1623 (ν<sub>C=N</sub>); HRESI-MS: m/z 368.90 (100%) [M-H]<sup>+</sup>.

### 1.3. 2,4-dibromo-6-((quinolin-8-ylimino)methyl)phenol (**L3H**)

Ligand **L3H** was synthesized following the same procedure adopted for **L1H** and **L2H**, using 8-aminoquinoline (0.29 g, 2 mmol) and 3,5-dibromosalicylaldehyde (0.56 g, 2 mmol) to give reddish orange powder. The ligand on recrystallization in dichloromethane obtained X-ray quality reddish orange single crystals. Yield: 0.76 g (89%). <sup>1</sup>H NMR (400 MHz, CDCl<sub>3</sub>, δ ppm): 9.03 (d, 1H, <sup>3</sup>J<sub>HH</sub> = 9.2 Hz, quin HC=N-), 8.99 (s, 1H, imine HC=N-), 8.24 (d, 1H, <sup>3</sup>J<sub>HH</sub> = 9.2 Hz, quin-H), 7.82 (d, 1H, <sup>3</sup>J<sub>HH</sub> = 9.2 Hz, quin-H), 7.80 (s, 1H, Ph-H), 7.63 (s, 1H, Ph-H), 7.60 (d, 1H, <sup>3</sup>J<sub>HH</sub> = 9.2 Hz, quin-H), 7.53 (t, 2H, <sup>3</sup>J<sub>HH</sub> = 7.2 Hz, quin-H); <sup>13</sup>C {<sup>1</sup>H} NMR (CDCl<sub>3</sub>): δ/ppm: 109.20, 113.59, 119.37, 120.49, 120.05, 126.49, 127.18, 129.25,

133.59,136.09,138.62, 141.88, 142.37, 150.76, 160.09, 161.76; IR  $\nu_{\max}/\text{cm}^{-1}$ : 3068 ( $\nu_{\text{OH}}$ ), 1609 ( $\nu_{\text{C=N}}$ ); HRESI-MS:  $m/z$  404.91 (100%)  $[\text{M-H}]^+$ .

***Nuclear magnetic resonance spectroscopy characterization of the Schiff base ligands***

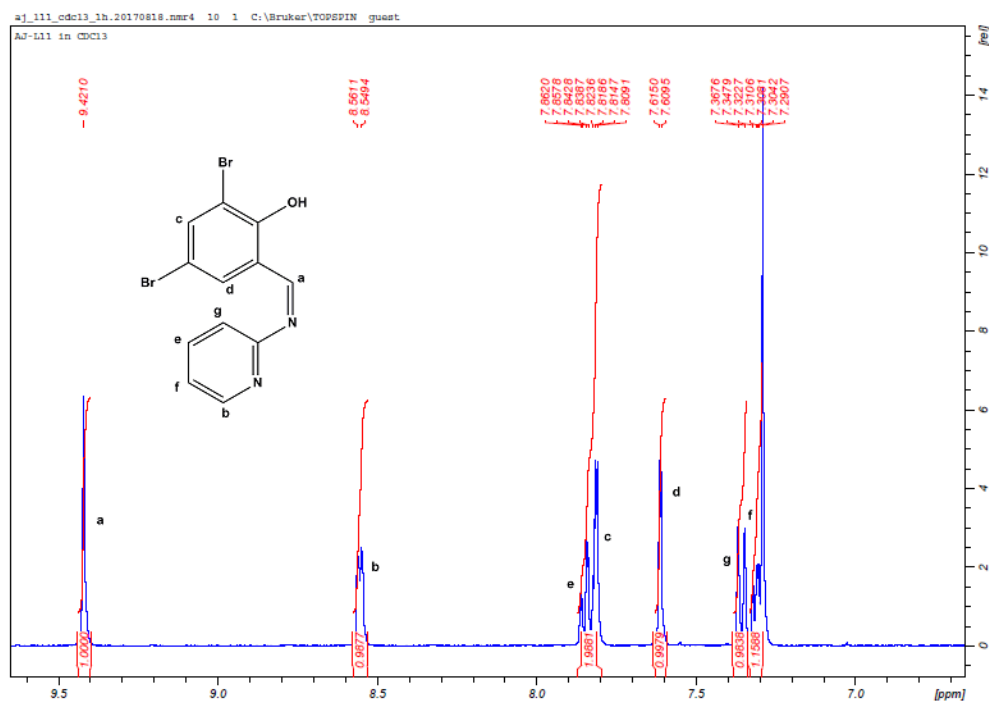


**Figure S1:**  $^1\text{H}$  NMR spectrum of ligand L1H in  $\text{CDCl}_3$  showing imine proton signal at 9.42 ppm.

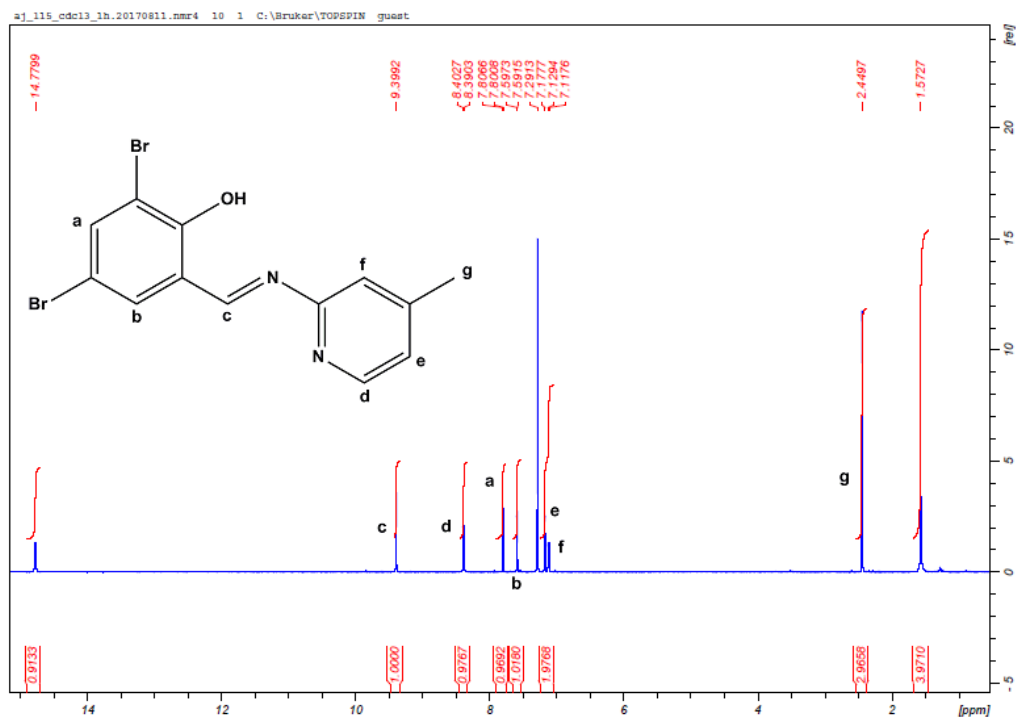


**Figure S2:** <sup>1</sup>H NMR spectrum of ligand **L2H** in CDCl<sub>3</sub> displaying the imine proton peak (c) at 9.39 ppm.

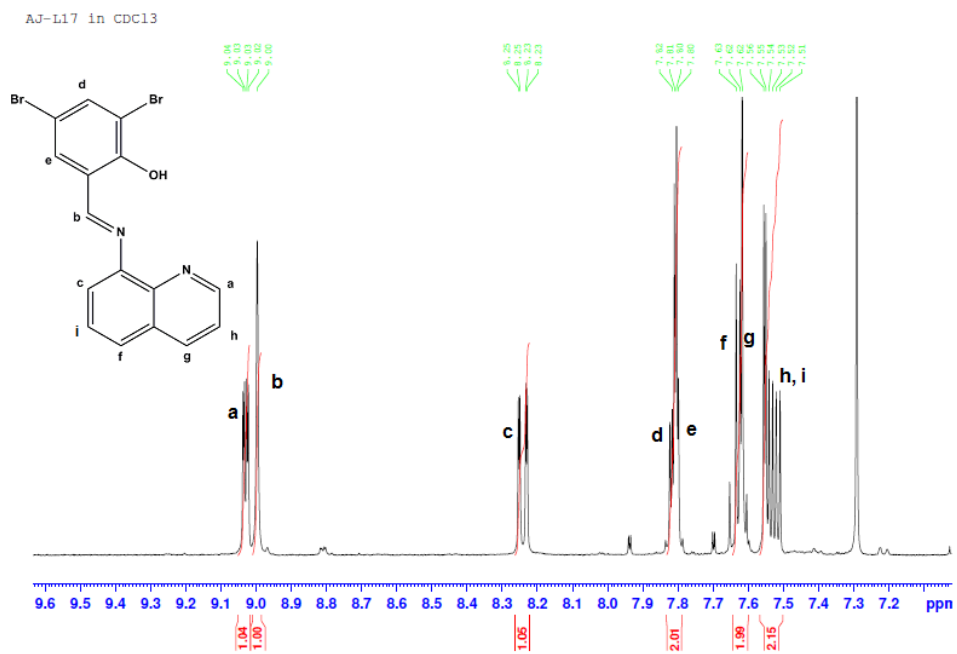


**Figure S3:** <sup>1</sup>H NMR spectrum of ligand **L3H** in CDCl<sub>3</sub> showing the presence of the imine (b) proton peak at 9.00 ppm.

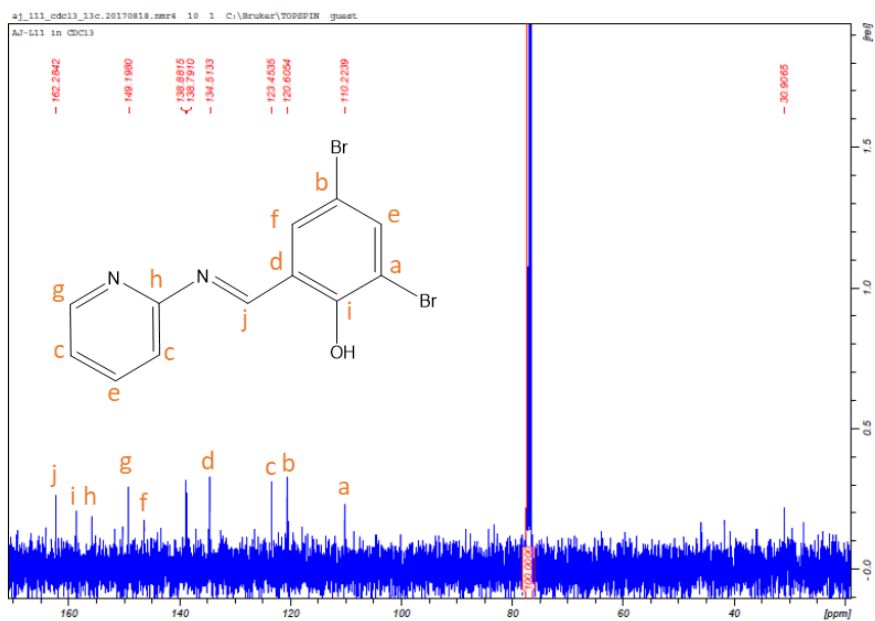


**Figure S4:**  $^{13}\text{C}$  NMR spectrum of ligand **L1H** in  $\text{CDCl}_3$  showing the presence of all carbons and the imine carbon at 162.3 ppm.

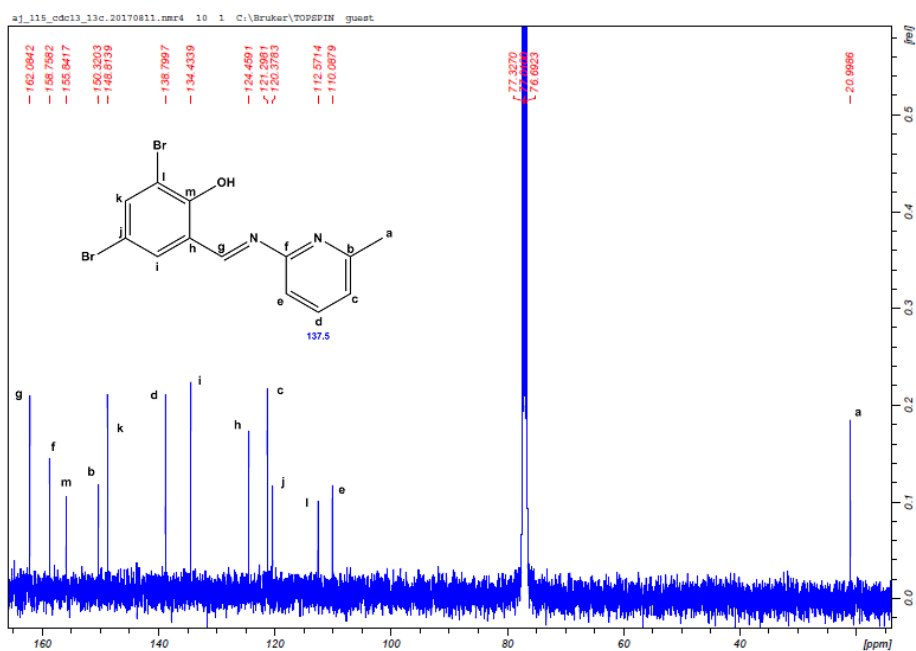


**Figure S5:**  $^{13}\text{C}$  NMR spectrum of ligand **L2H** in  $\text{CDCl}_3$  showing the imine carbon peak (g) at 162.1 ppm.

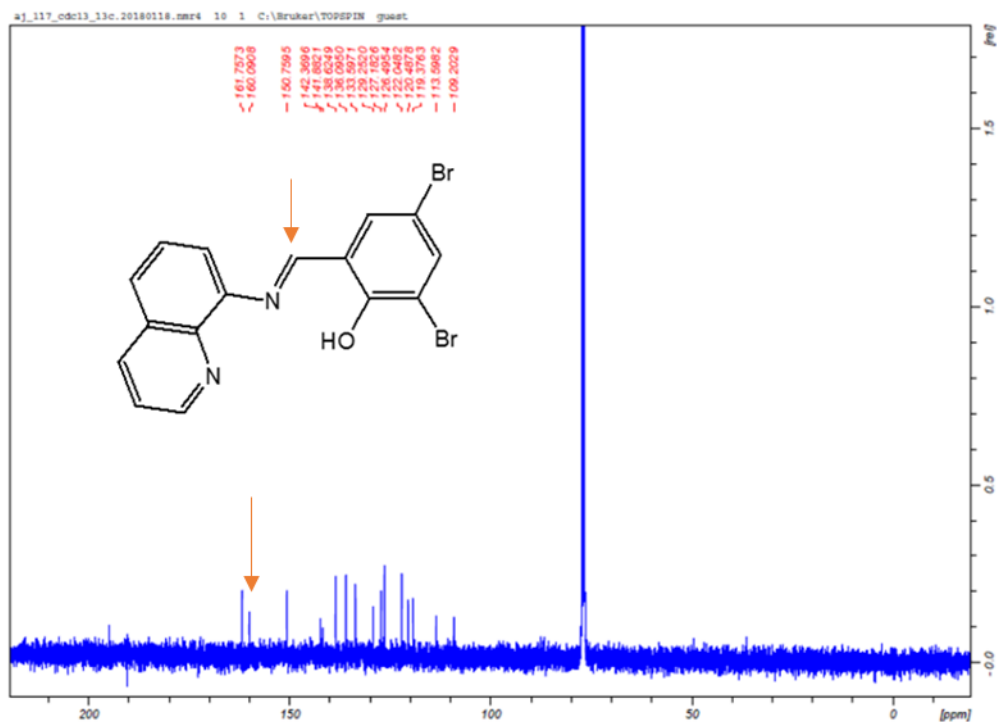


**Figure S6:**  $^{13}\text{C}$  NMR spectrum of ligand **L3H** in  $\text{CDCl}_3$  showing the diagnostic imine carbon signal at 161.8 ppm.

**FTIR spectroscopic analyses of the Schiff base ligands (L1H-L3H) and their metal complexes**

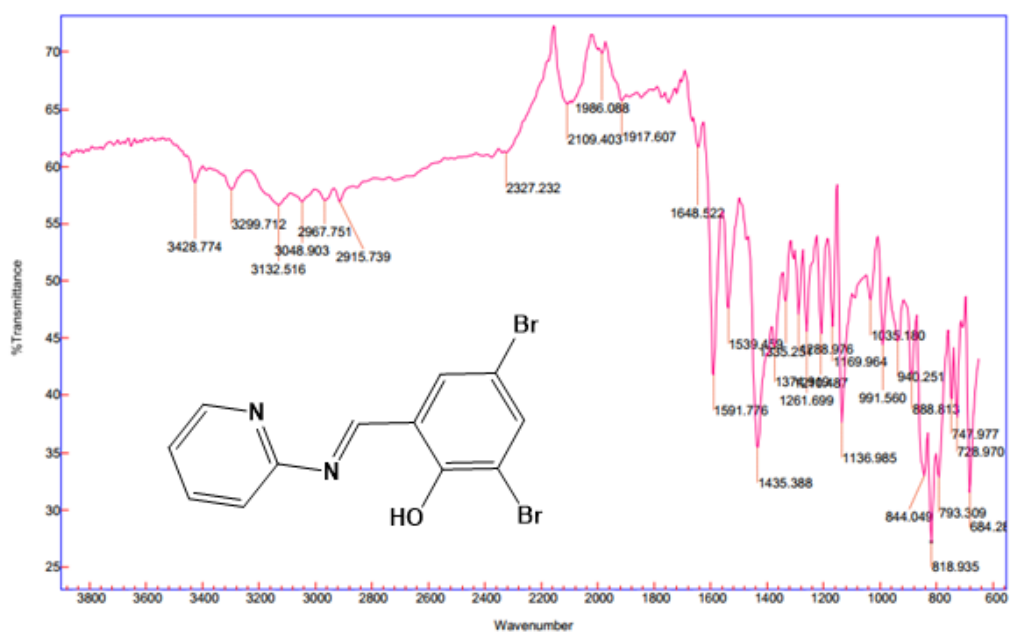


**Figure S7:** FTIR spectrum of the Schiff base ligand **L1H** showing the presence of  $\nu_{(C=N)}$  at  $1592\text{ cm}^{-1}$ .

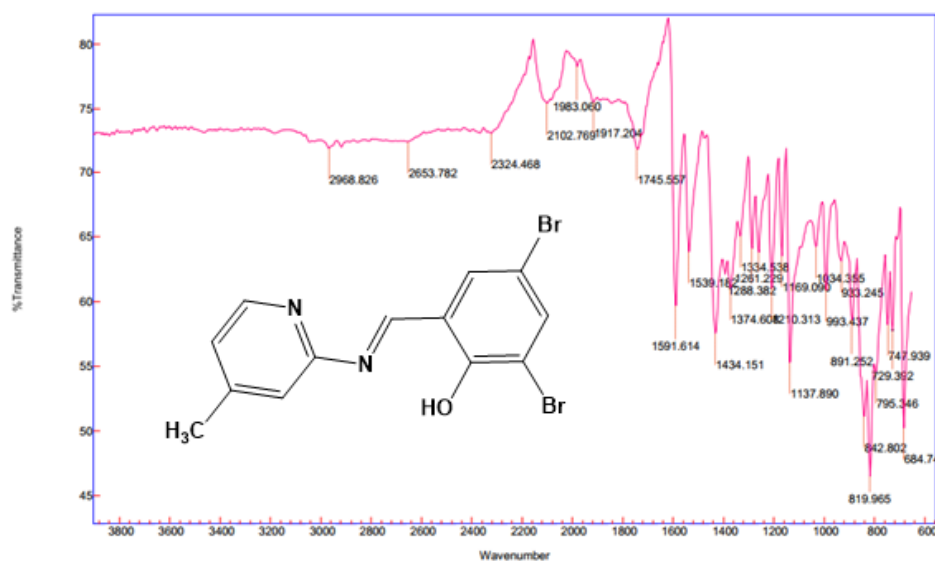


**Figure S8:** FTIR spectrum of the Schiff base ligand **L2H** showing the presence of  $\nu_{(C=N)}$  at  $1591\text{ cm}^{-1}$ .

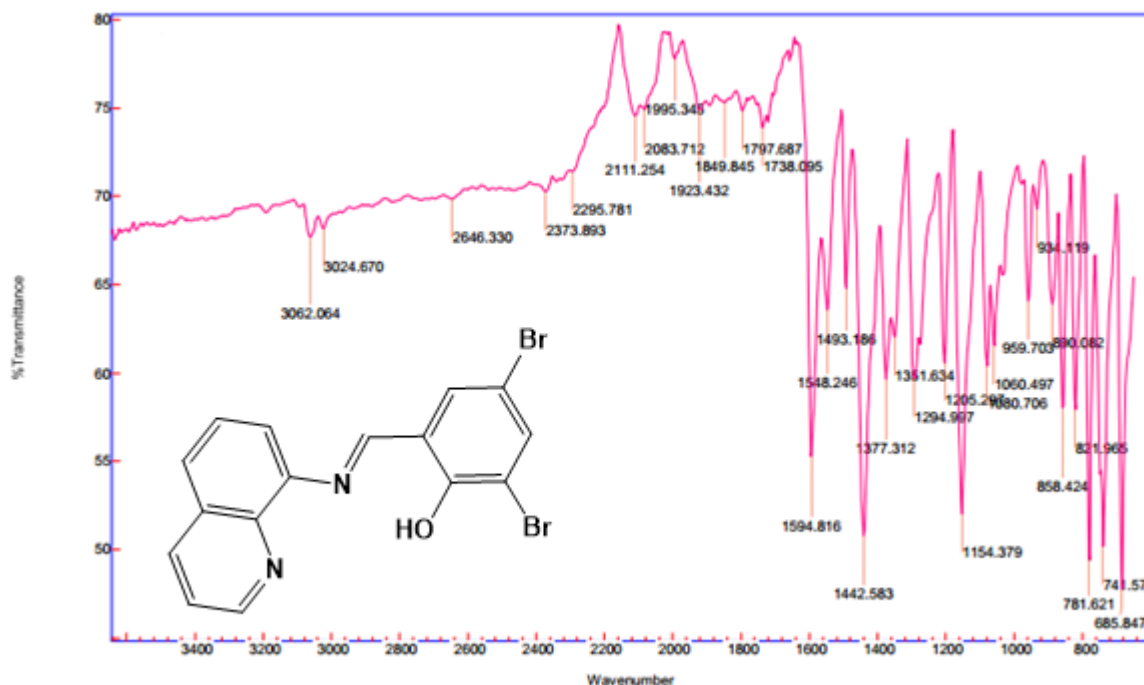


**Figure S9:** FTIR spectrum of the Schiff base ligand **L3H** showing the presence of  $\nu_{(C=N)}$  and  $\nu_{(O-H)}$  and  $1594\text{ cm}^{-1}$  and  $3062\text{ cm}^{-1}$  respectively.

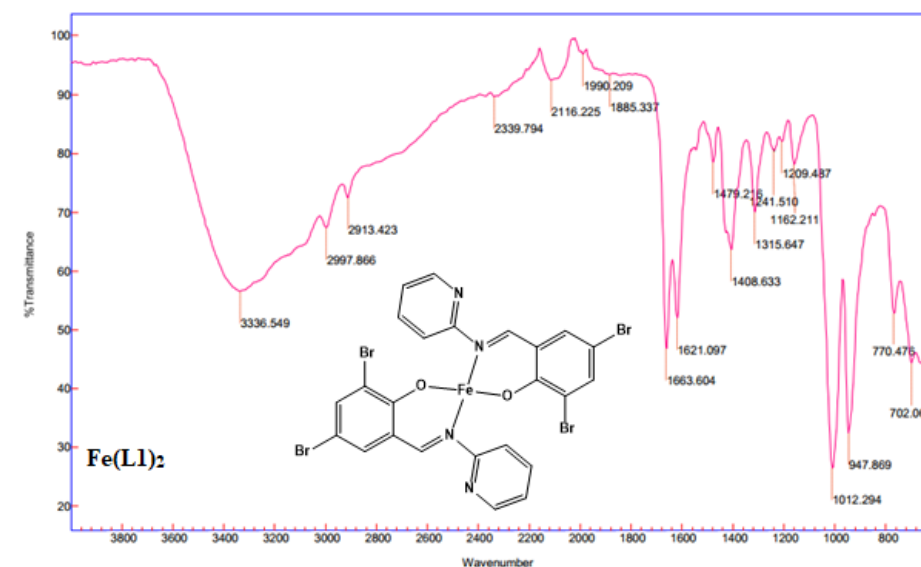


**Figure S10:** FTIR spectrum of  $\text{Fe1}$  showing the presence of  $\nu(\text{C}=\text{N})$  at  $1663.60 \text{ cm}^{-1}$ .

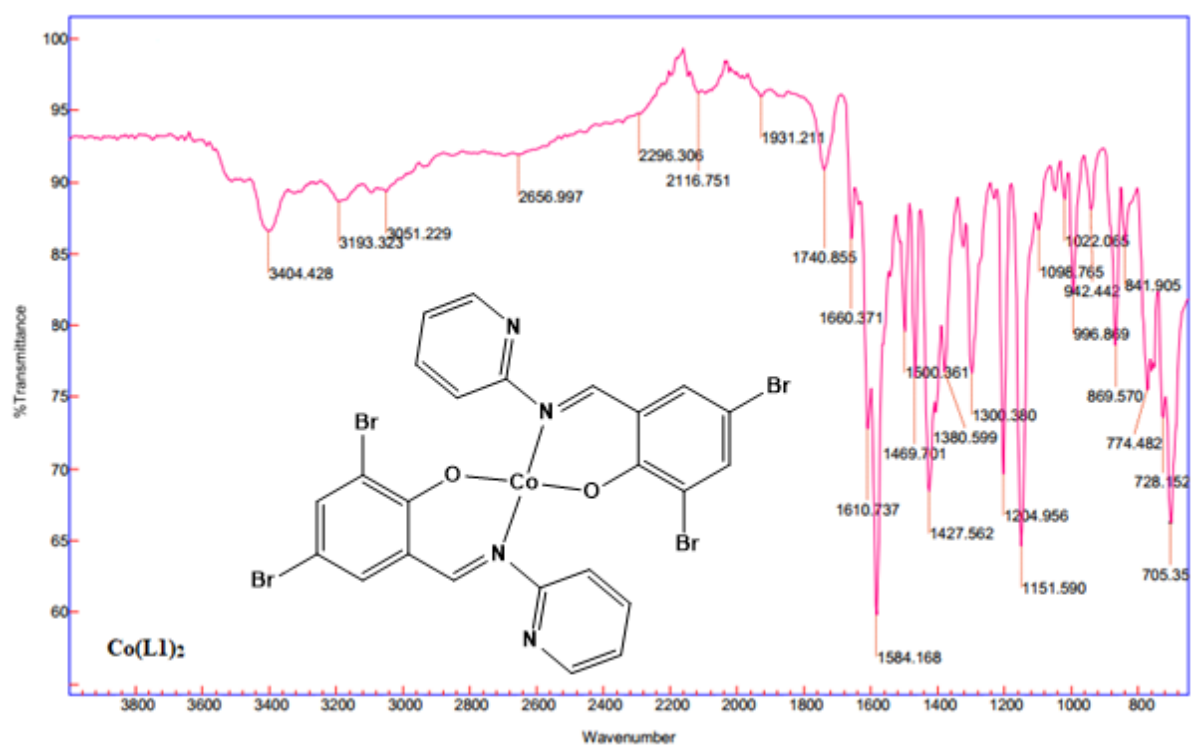


**Figure S11:** FTIR spectrum of  $\text{Co1}$  showing the  $\nu(\text{C}=\text{N})$  stretching frequency at  $1584 \text{ cm}^{-1}$ .

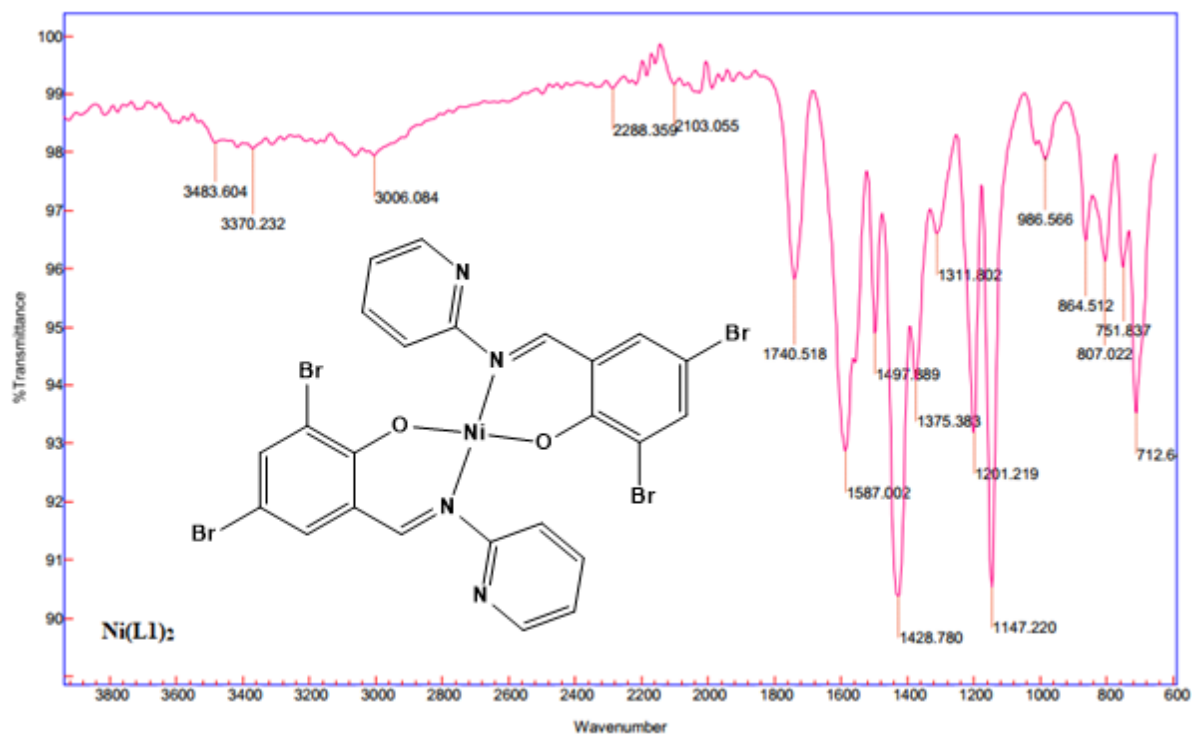


**Figure S12:** FTIR spectrum of **Ni1** showing the sharp peak at  $1587.02\text{ cm}^{-1}$  corresponding to the  $\nu_{(\text{C}=\text{N})}$  stretching frequency.

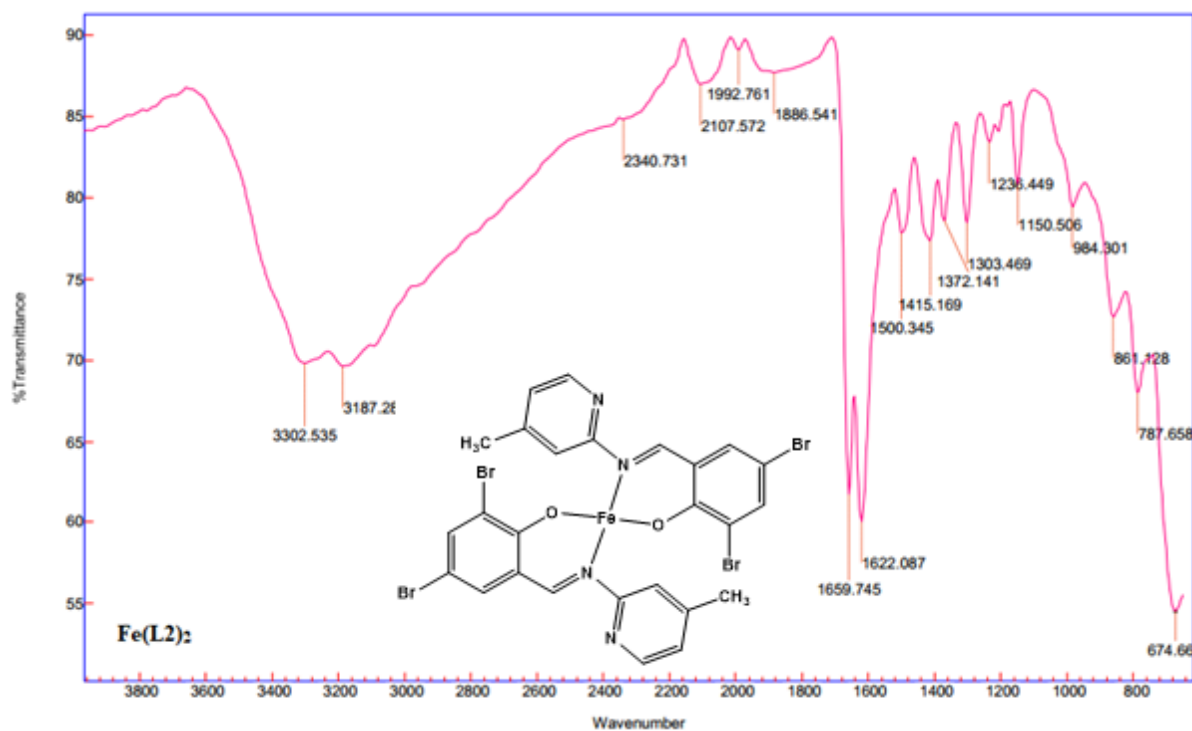


**Figure S13:** FTIR spectrum of **Fe2** showing the  $\nu_{(\text{C}=\text{N})}$  stretching frequency at  $1659.74\text{ cm}^{-1}$ .

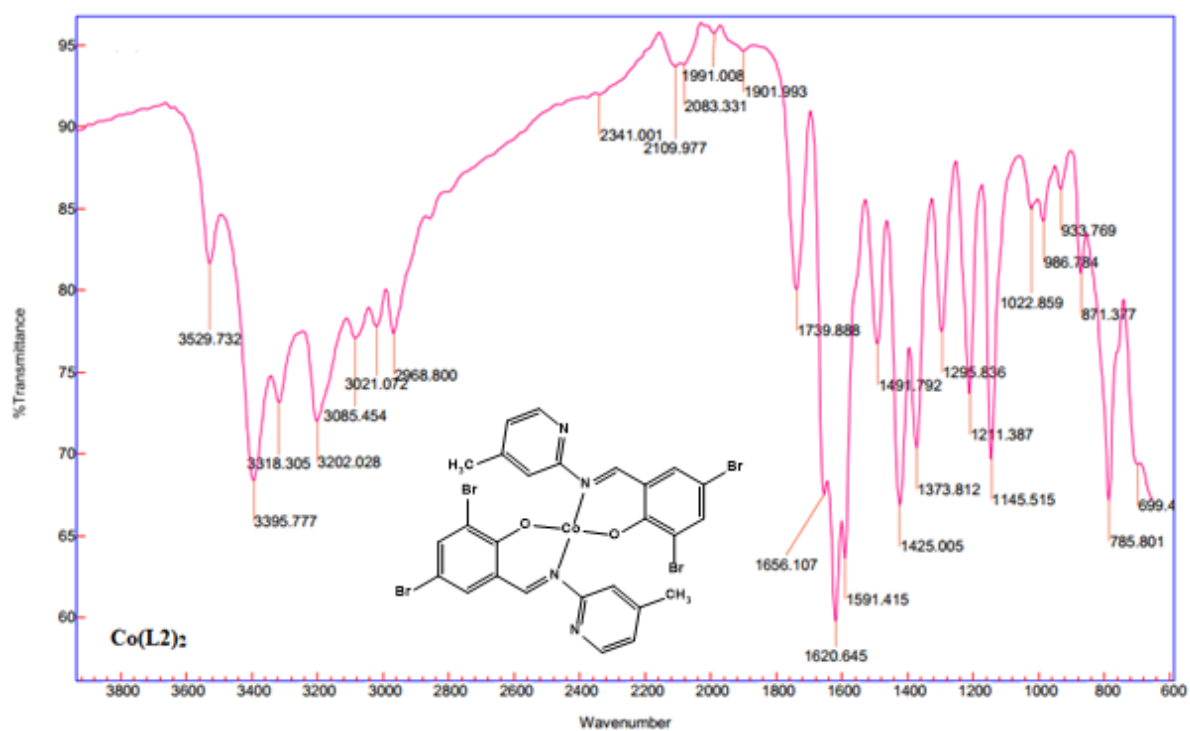


**Figure S14:** FTIR spectrum of **Co2** showing the  $\nu_{(C=N)}$  stretching frequency at 1620.64 cm<sup>-1</sup>.

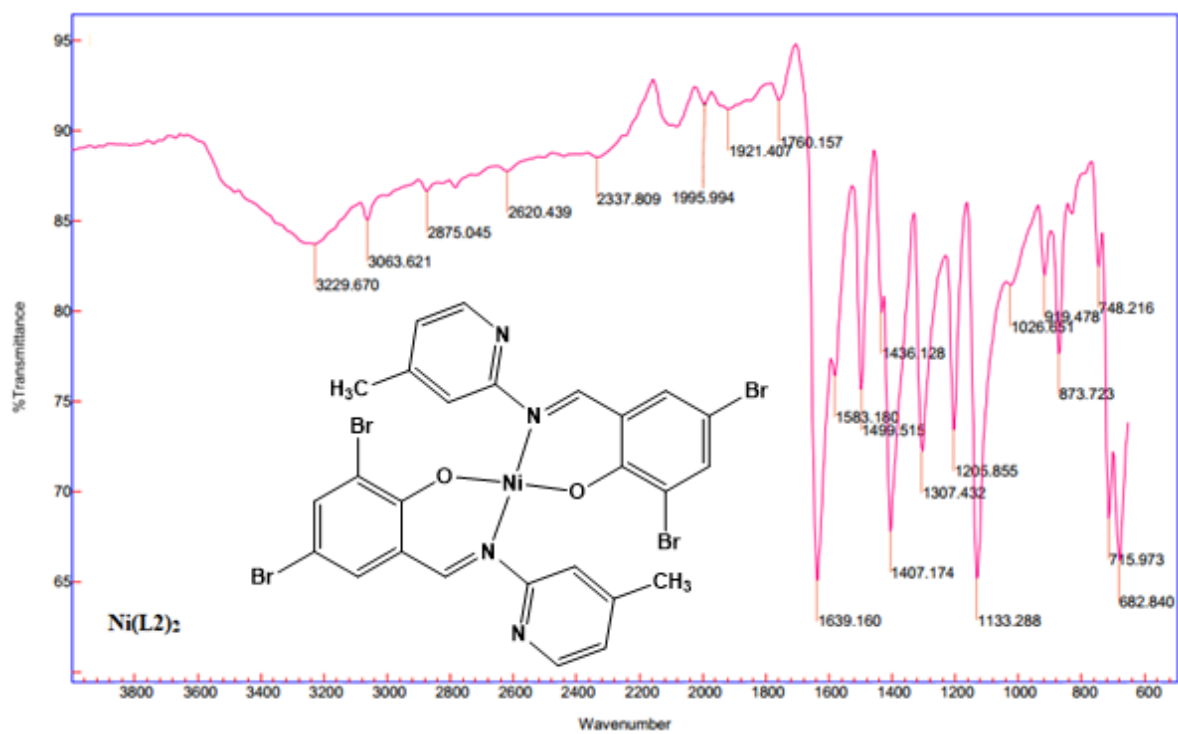


**Figure S15:** FTIR spectrum of **Ni2** showing a long and sharp peak at  $1639.16\text{ cm}^{-1}$  which is a diagnostic peak of  $\nu(\text{C}=\text{N})$  stretching frequency.

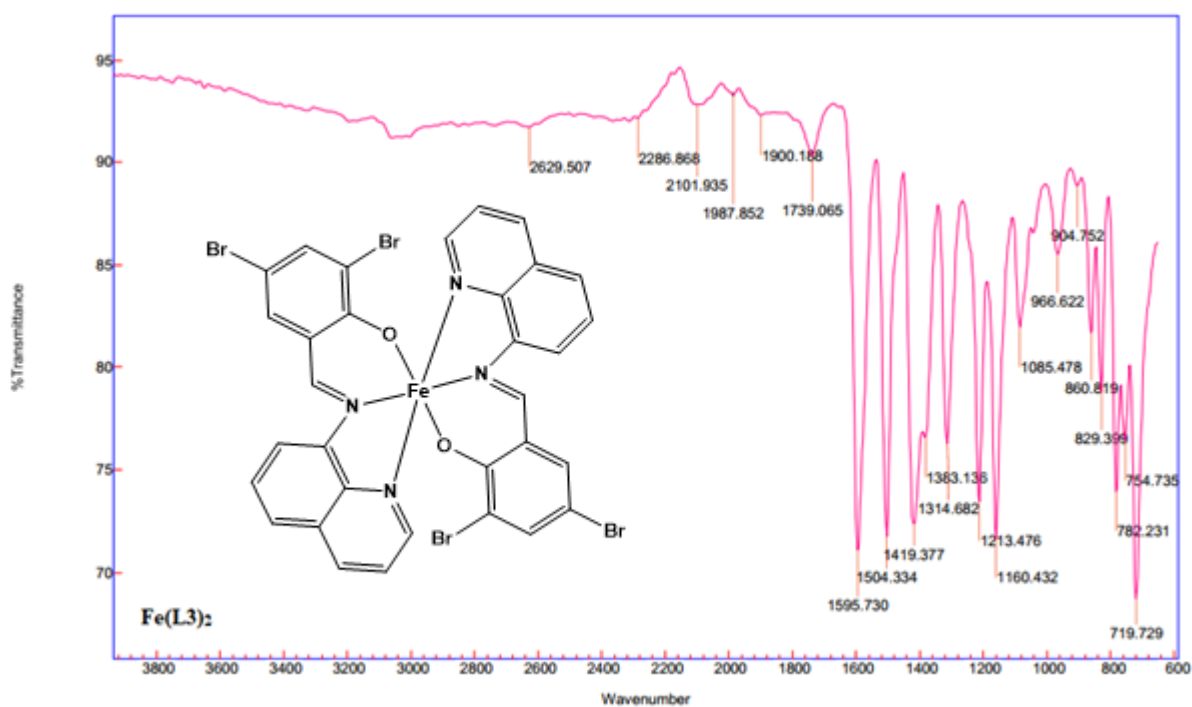


**Figure S16:** FTIR spectrum of **Fe3** showing the  $\nu(\text{C}=\text{N})$  stretching frequency at  $1595\text{ cm}^{-1}$ .

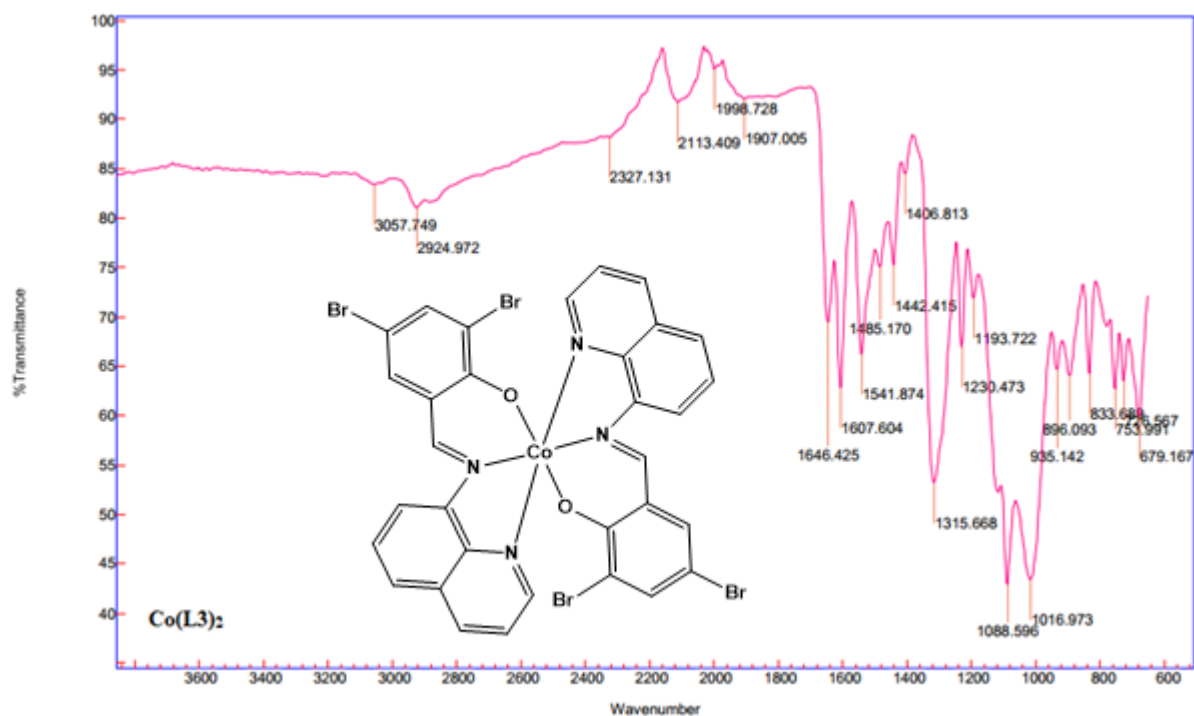


**Figure S17:** FTIR spectrum of **Co3** showing the  $\nu_{(\text{C}=\text{N})}$  stretching frequency at a higher wavenumber of  $1646.43 \text{ cm}^{-1}$ .

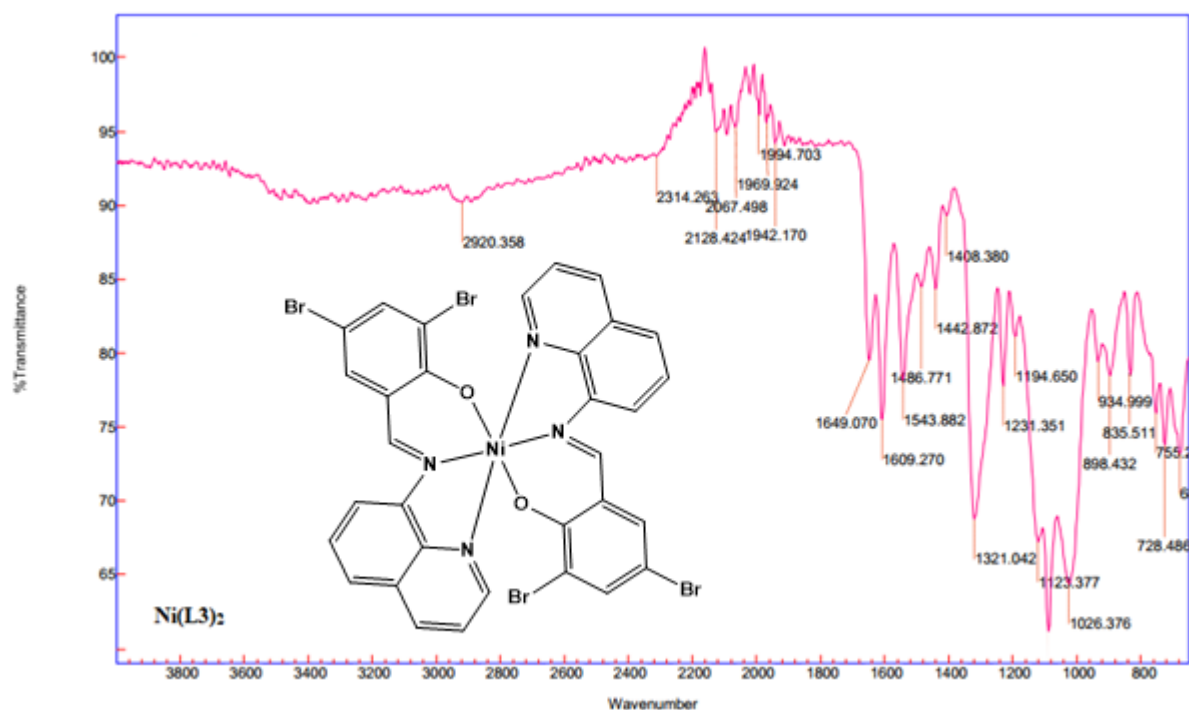


**Figure S18:** FTIR spectrum of **Ni3** revealing the presence of the  $\nu_{(\text{C}=\text{N})}$  stretching frequency at  $1609.27 \text{ cm}^{-1}$  and the absence of the O-H proton upon complexation.

**Mass spectrometric analyses of the Schiff base ligands and their metal complexes**

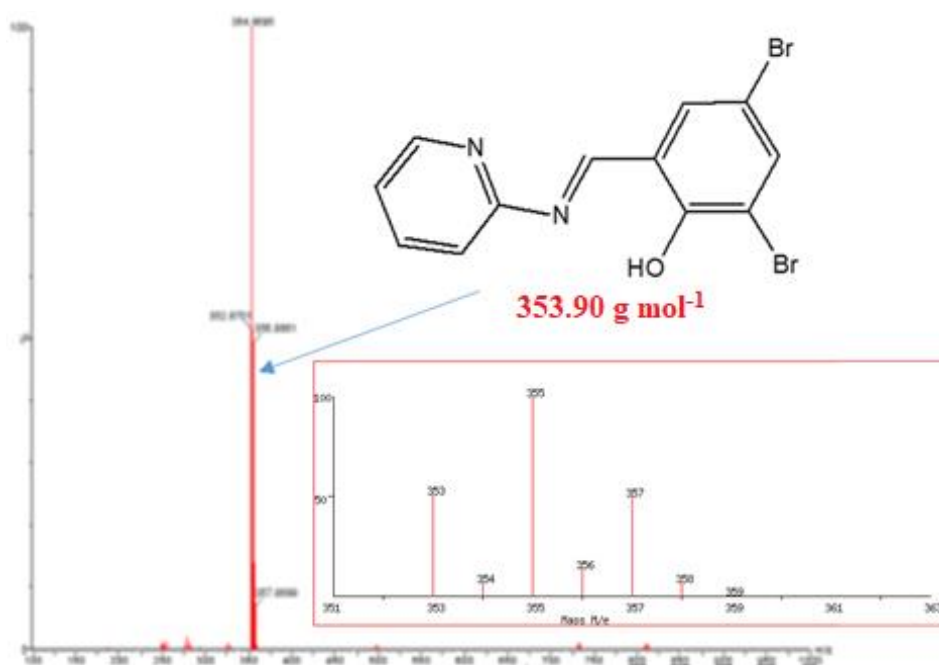


**Figure S19:** Mass spectrum of ligand **L1H** showing the ligand's [M]<sup>+</sup> molecular ion peak at 354.34 amu and its predicted isotopic distribution inserted.

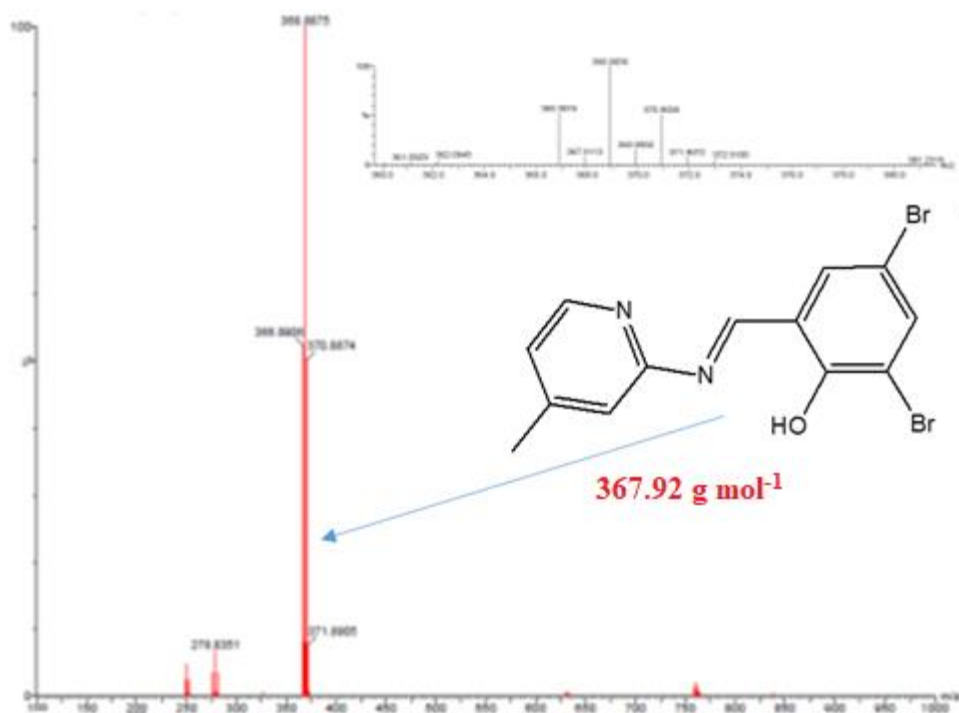


**Figure S20:** Mass spectrum of ligand **L2H** (HR-MS inserted) illustrating the ligand's molecular ion peak  $[M]^+$  at 368.04 amu.

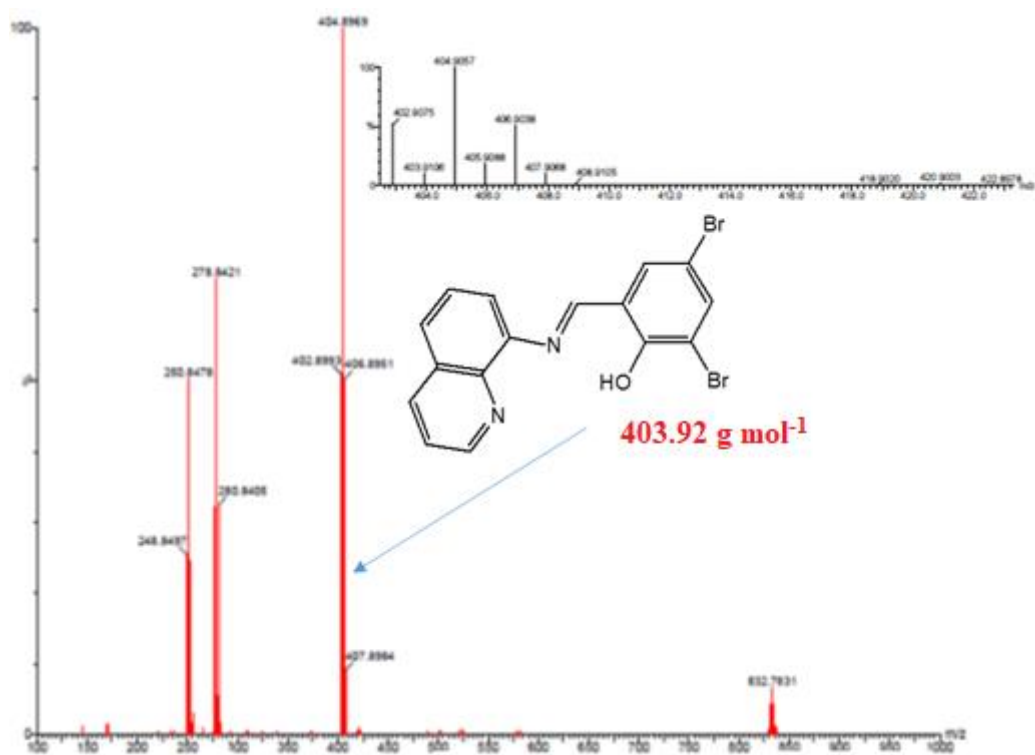


**Figure S21:** Mass spectrum of ligand **L3H** (HR-MS inserted) showing the ligand's base peak  $[M]^+$  at 404.84 amu.

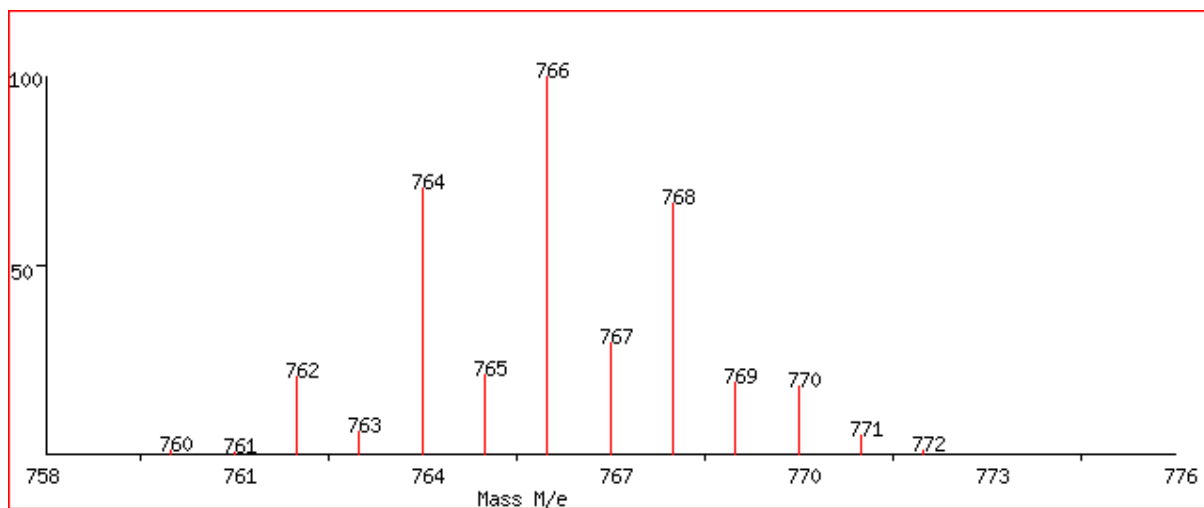
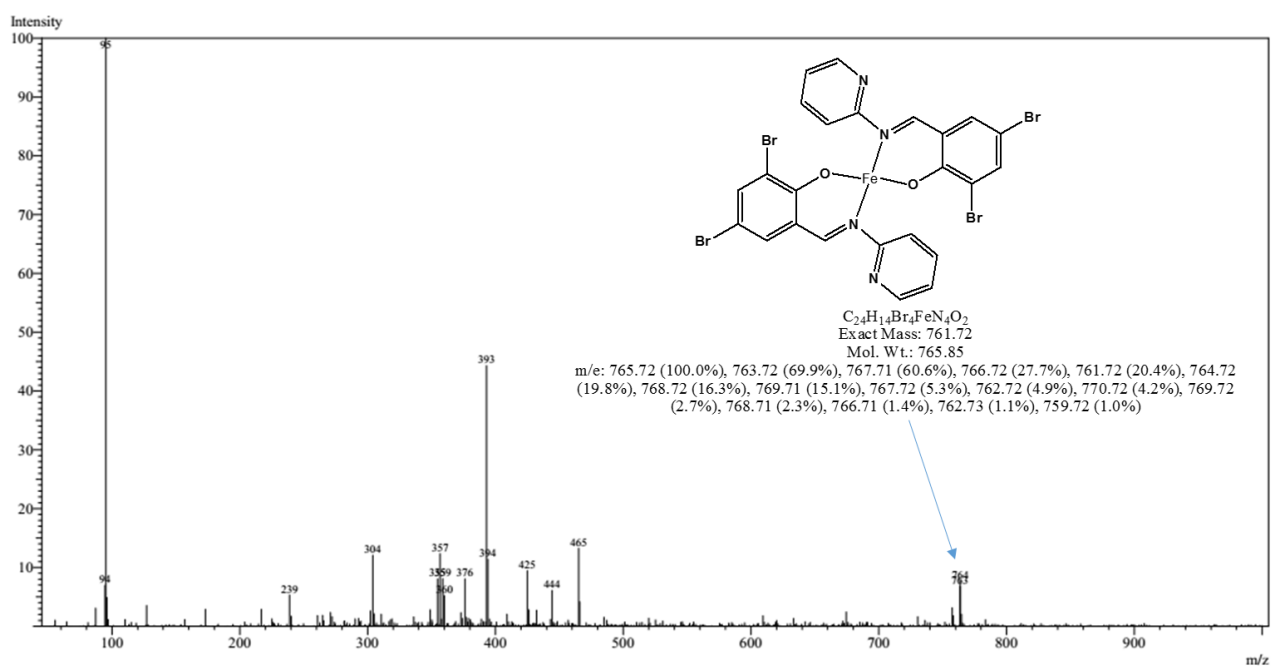


**Figure S22:** Mass spectrum of complex **Fe1** showing the formation of the *bis*-chelated complex by the peak at 364.00 (10 %) and its predicted isotopic distribution at  $m/z = 765$  amu.

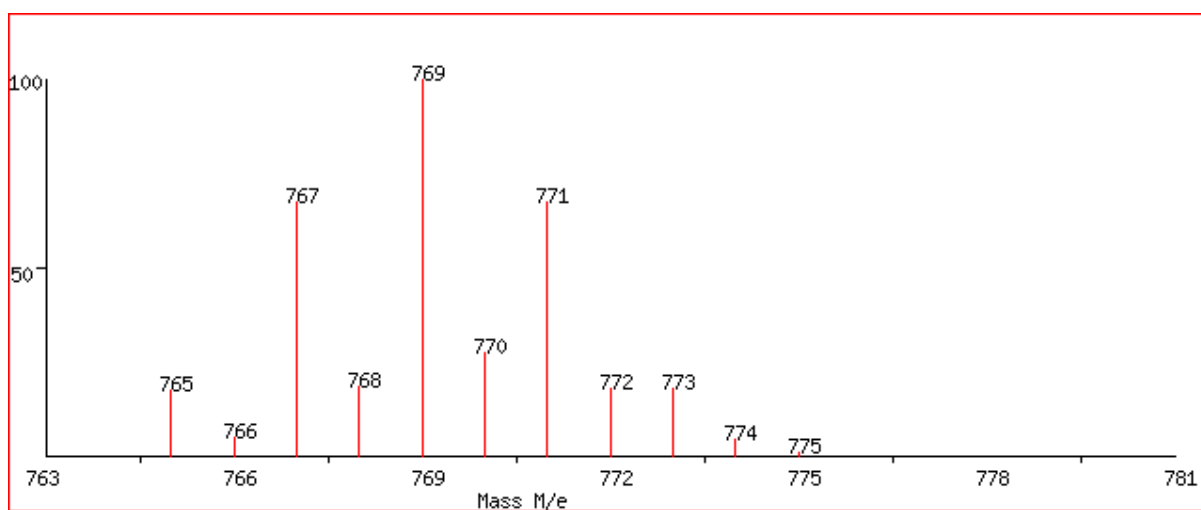
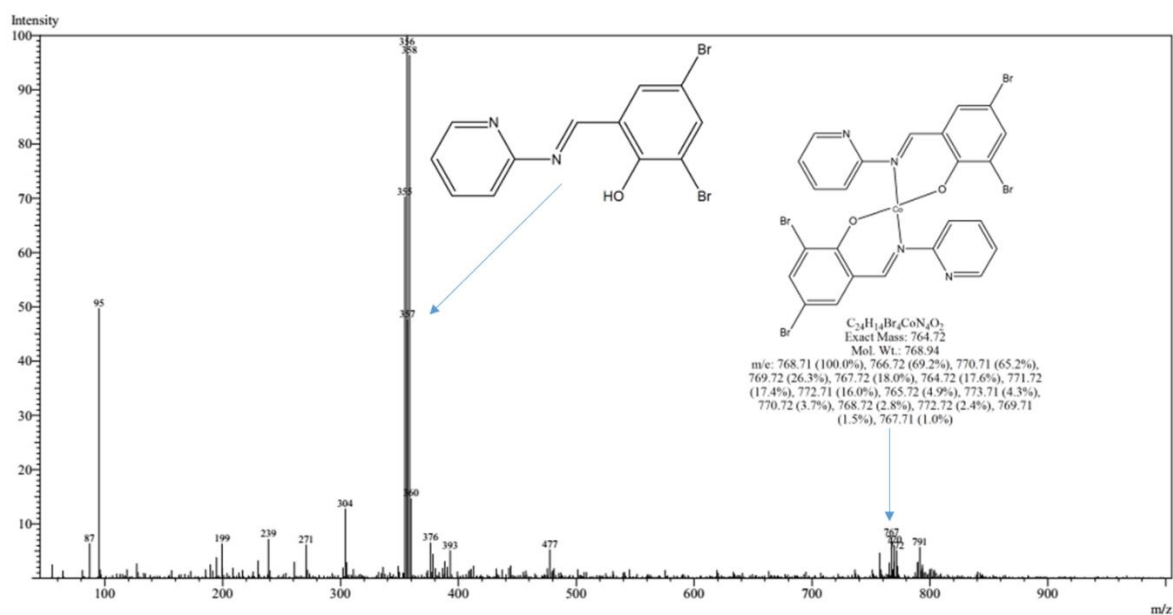


**Figure S23:** ESI Mass spectrum of complex **Co1** showing a peak at 767.00 amu corresponding to  $[\text{Co}(\mathbf{L1})_2]^+$  fragment and its simulated isotopic distribution at  $m/z = 769$  amu.

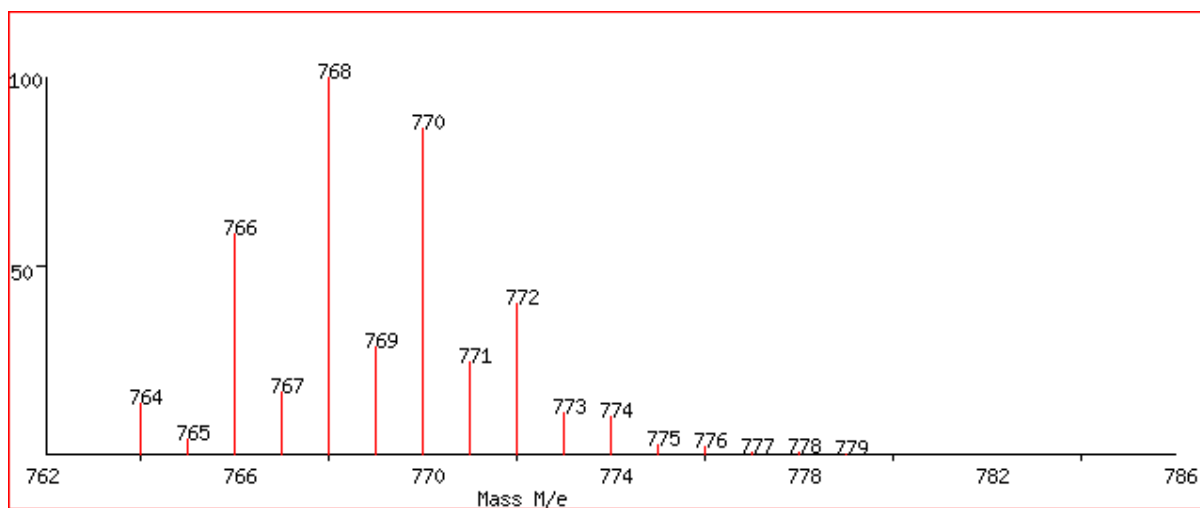
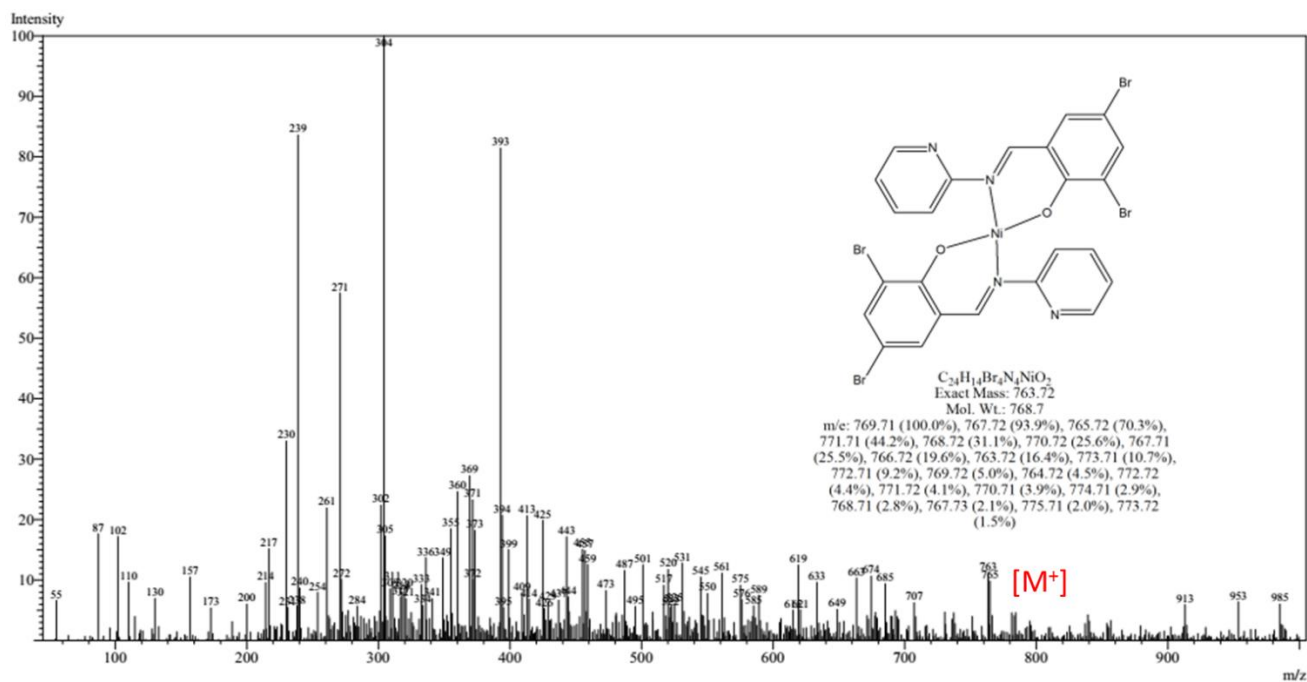


**Figure S24:** Mass spectrum of complex **Ni1** showing the peak  $[\text{Ni}(\text{L1})_2]^+$  fragment at 763.00 amu and its predicted isotopic distribution at  $m/z = 768$  amu.

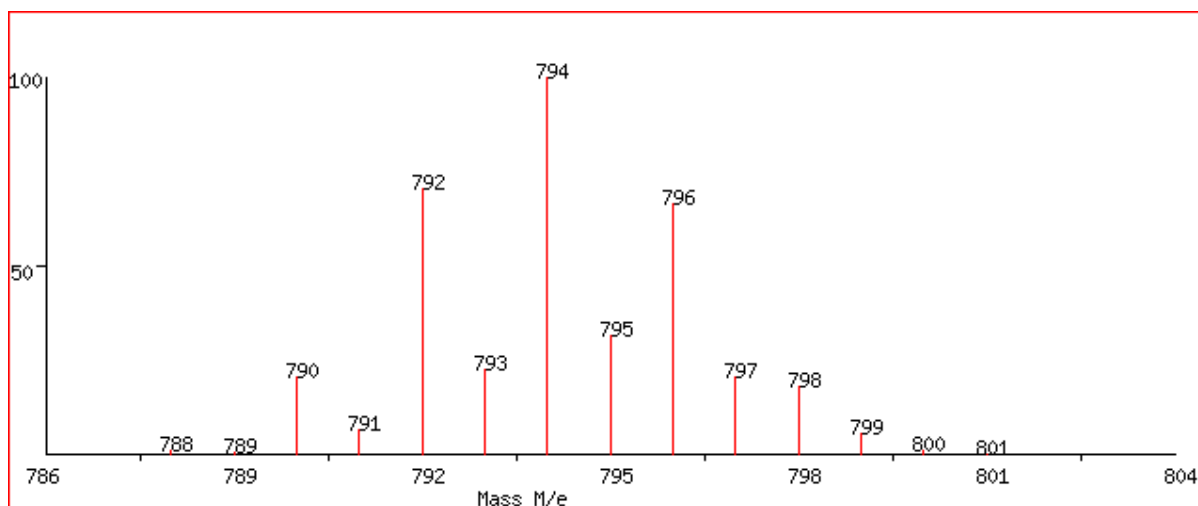
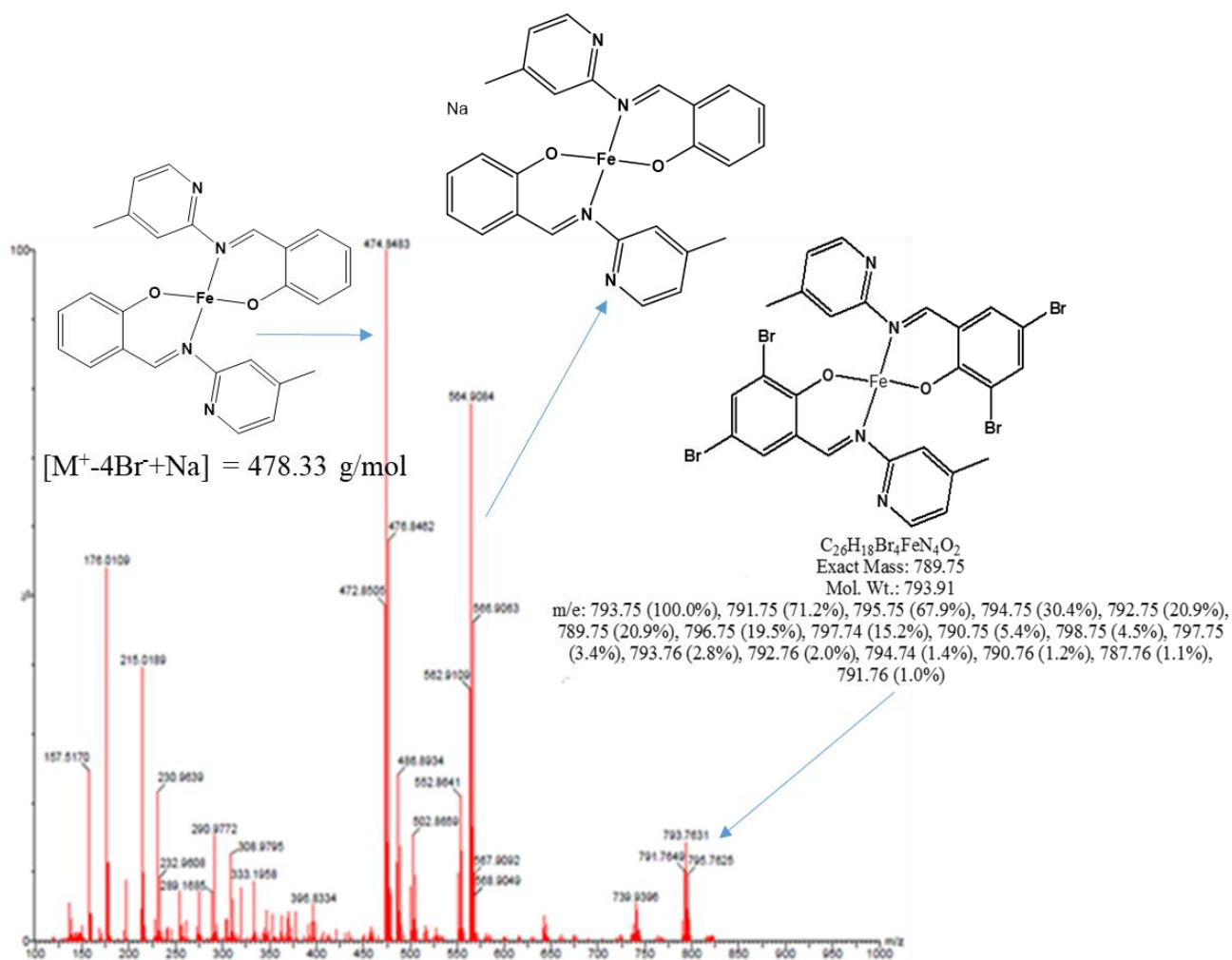


**Figure S25:** ESI Mass spectrum of complex **Fe2** showing the  $[M^+]$  peak at 793.76 amu and base peak at 474.14 amu corresponding to  $[Fe(L2)_2 - 4Br^-]^+$  fragment. Its predicted isotopic distribution at  $m/z = 794$  amu is also illustrated.

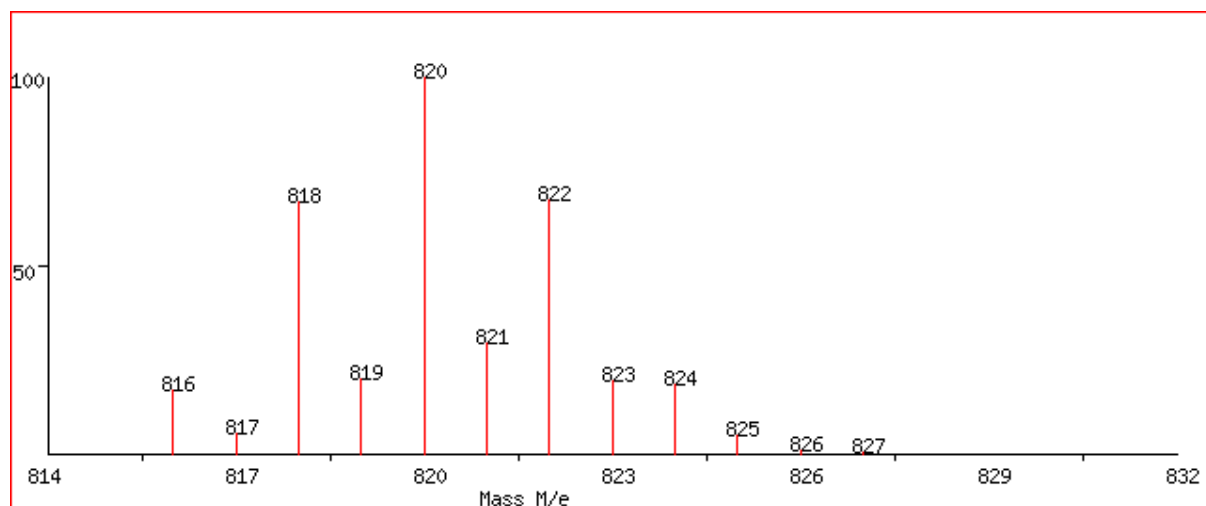
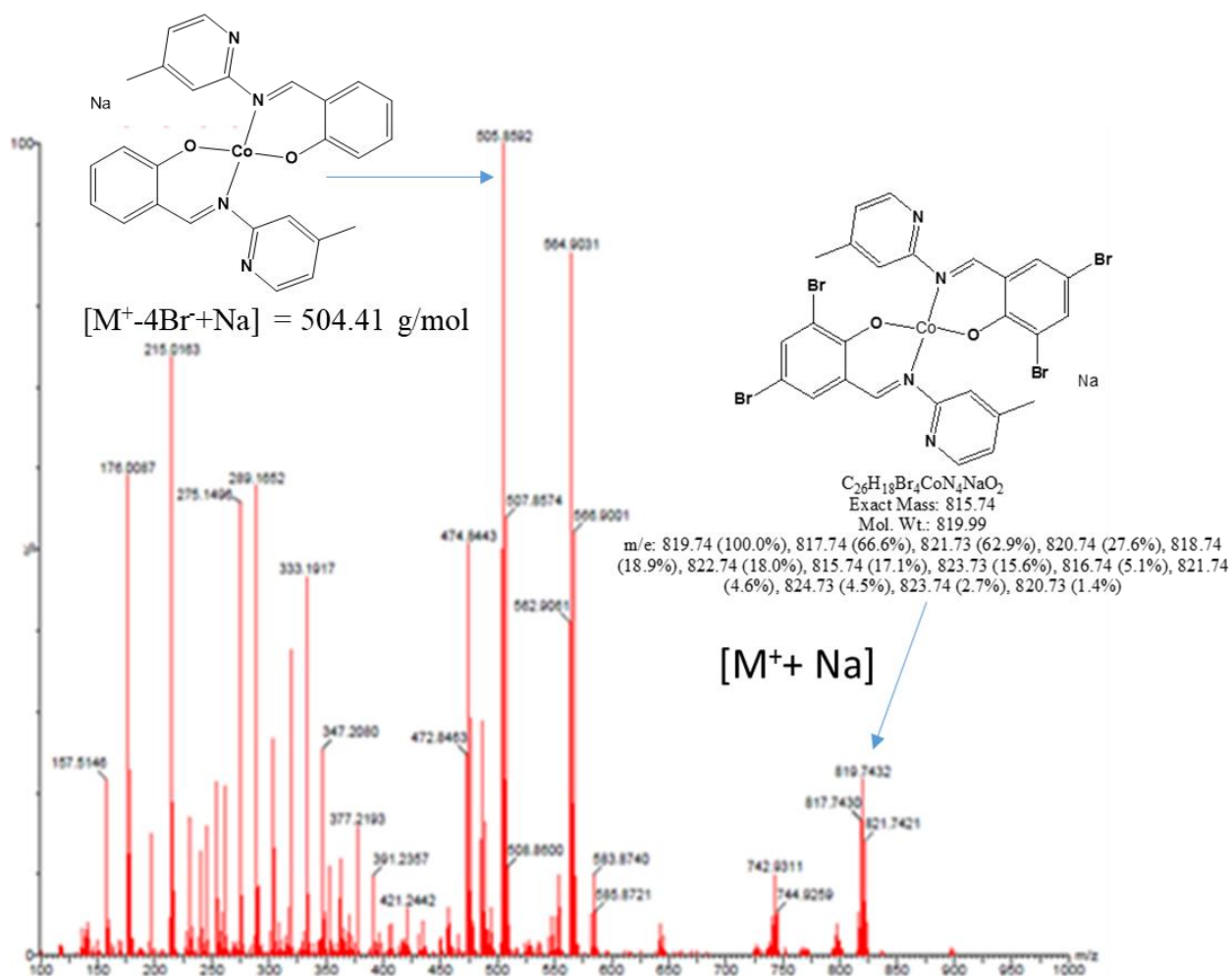


**Figure S26:** ESI Mass spectrum of complex **Co2** showing the  $[M^+]$  peak at 819.74 amu (25 %) and its predicted isotopic distribution at  $m/z = 820$  amu.

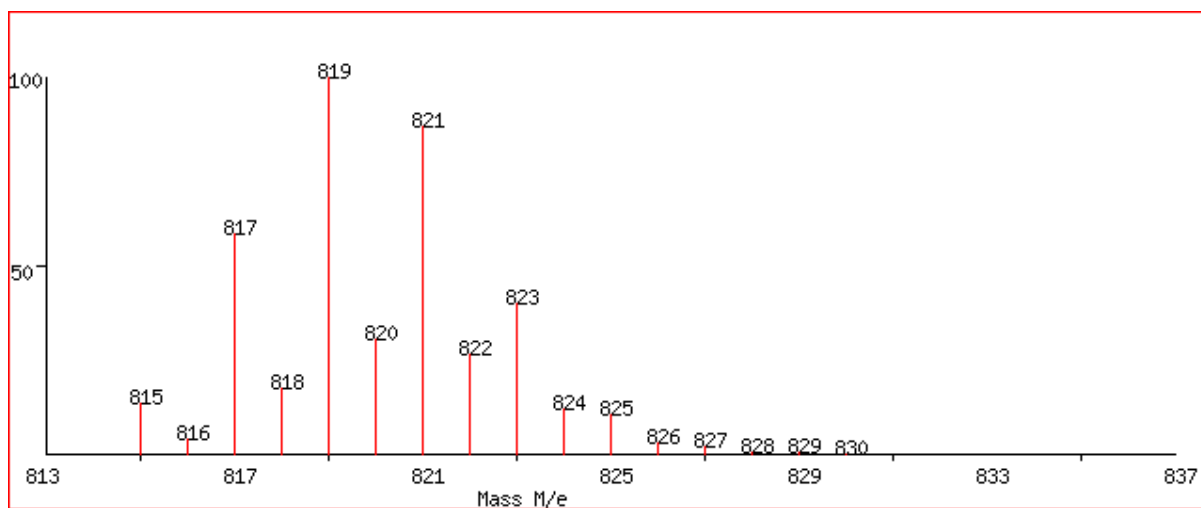
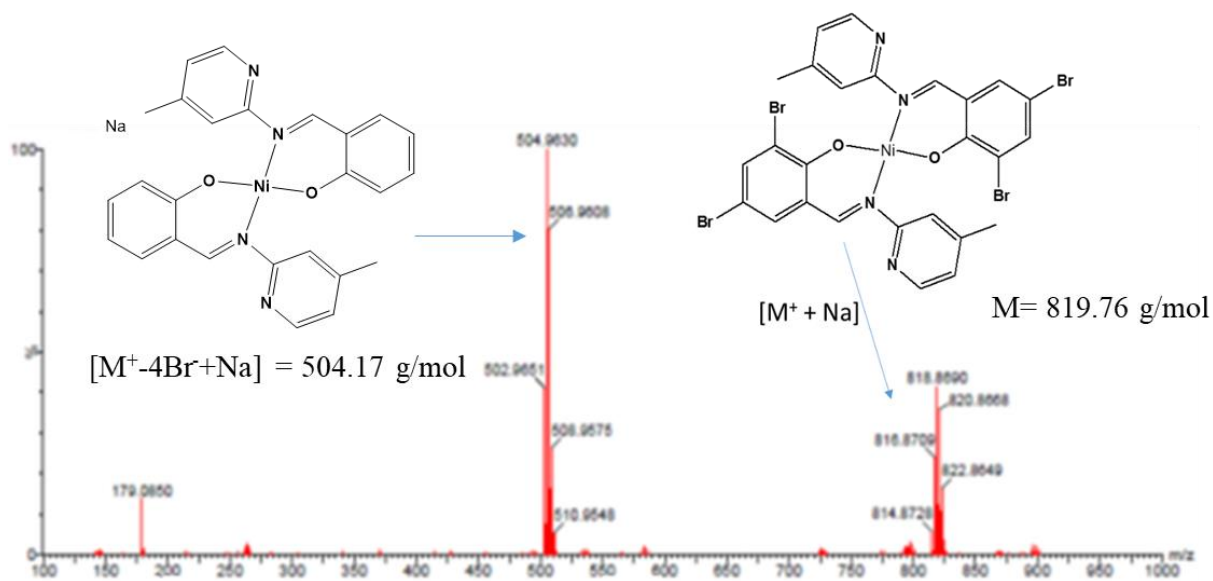


**Figure S27:** Mass spectrum of complex **Ni2** showing the  $[Ni(L2)_2]^+$  fragment at 818.86 amu (30 %) and its predicted isotopic distribution at  $m/z = 819$  amu. The peak at  $m/z = 504.17$  amu corresponds to  $[Ni(L2)_2 + Na - 4Br^-]^+$  molecular ion peak.

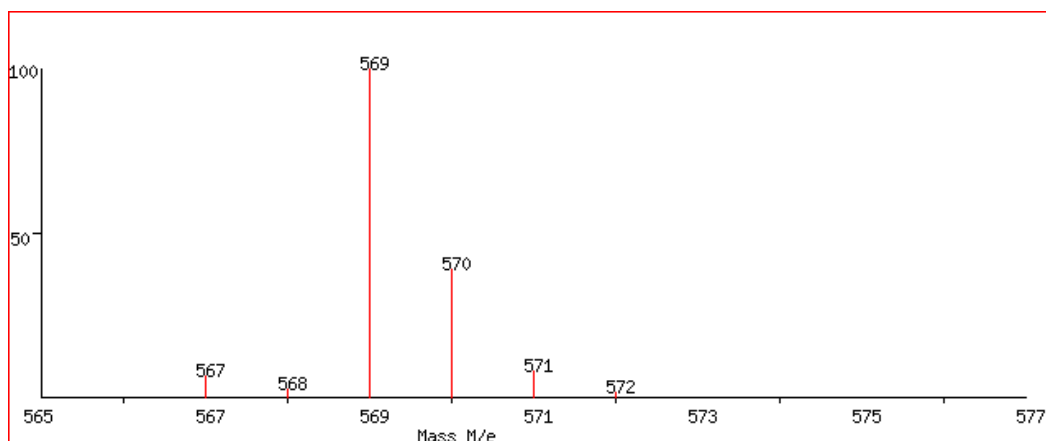
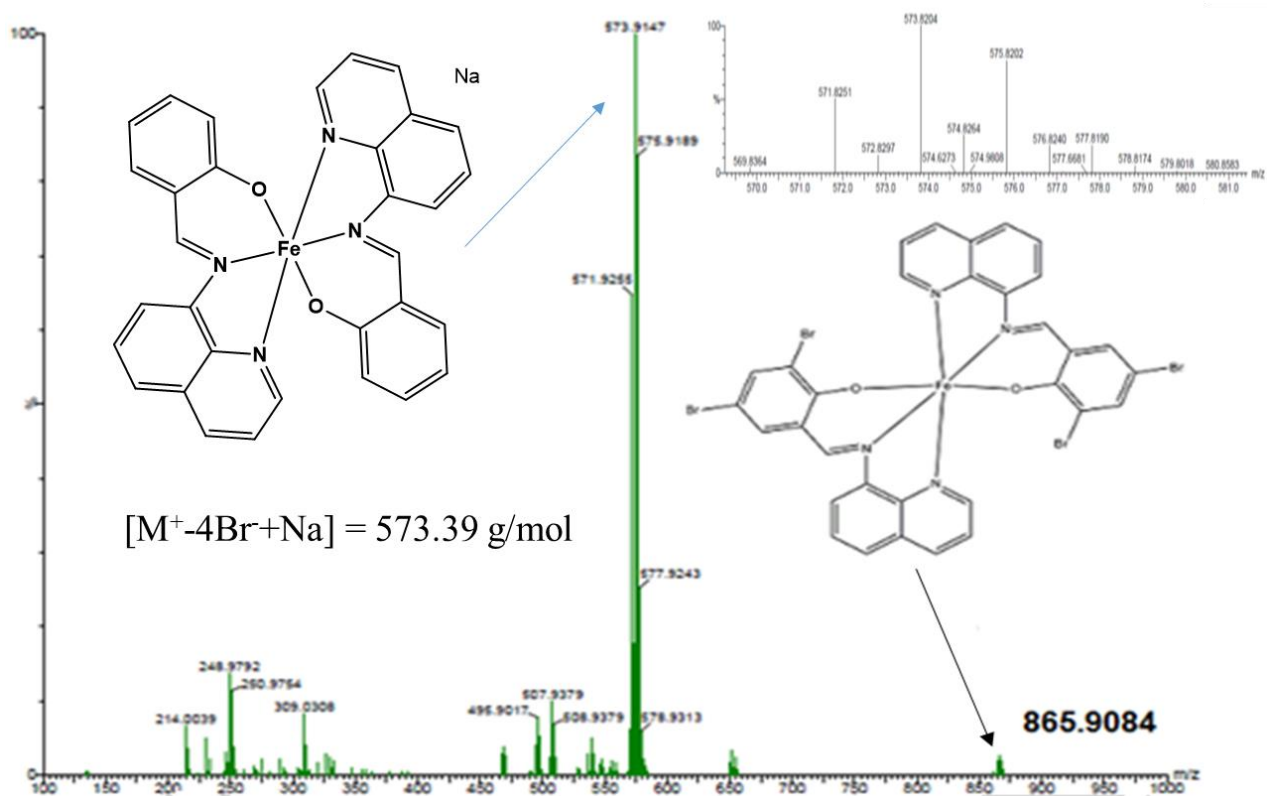


**Figure S28:** LR-MS and HR-MS ESI (inserted) mass spectra of complex **Fe3** showing the base peak at 573.91 amu (100 %) corresponding to  $[Fe(L3)_2 + Na - 4Br^-]^+$  fragment and the isotopic distribution of the molecular ion peak at  $m/z = 569$  amu.

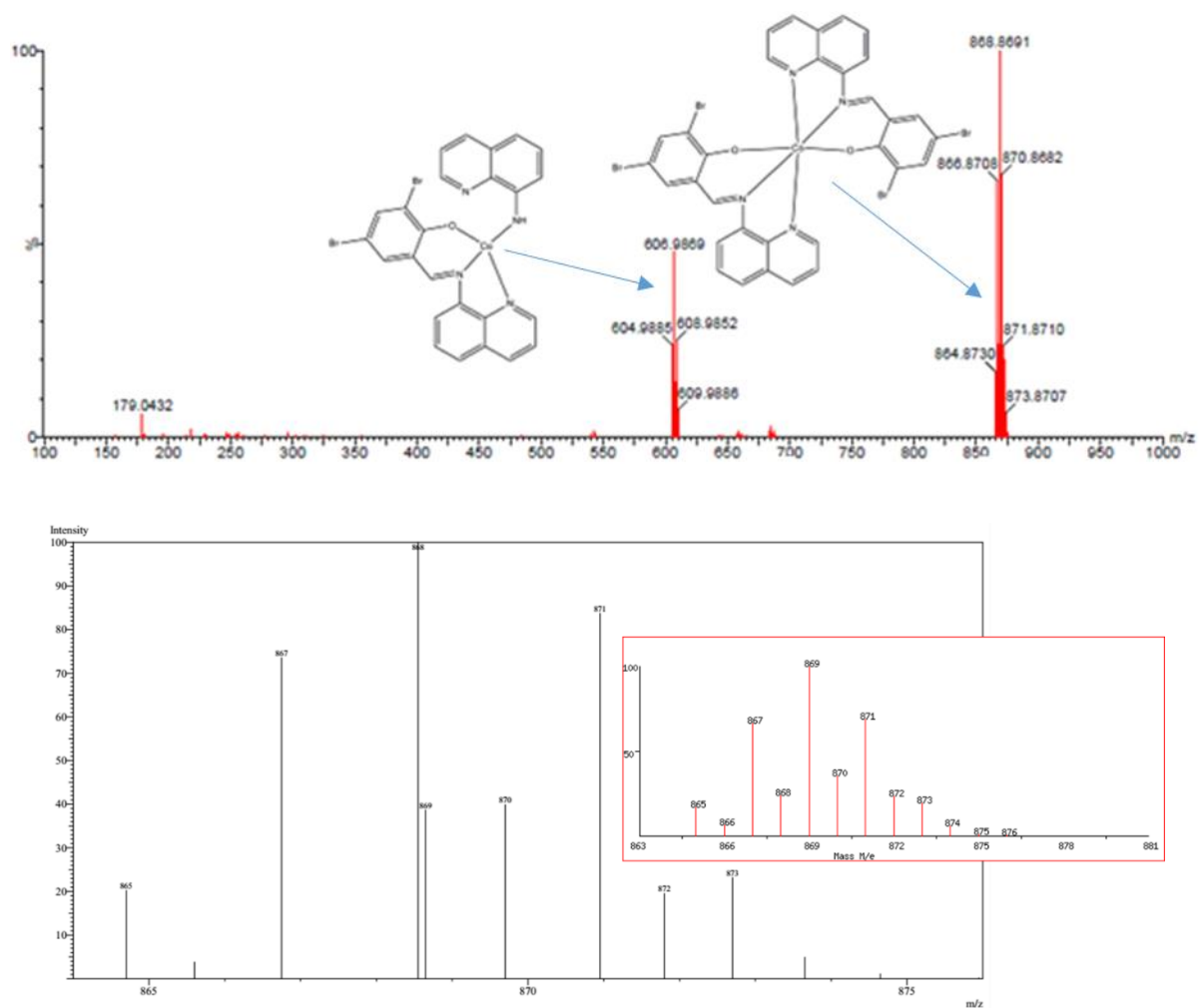


**Figure S29:** Mass spectrum of complex **Co3** showing the formation of a *bis*-chelated cobalt complex at 868.87 amu and the combination of experimental and the predicted isotopic distribution of the molecular ion peak of the complex.

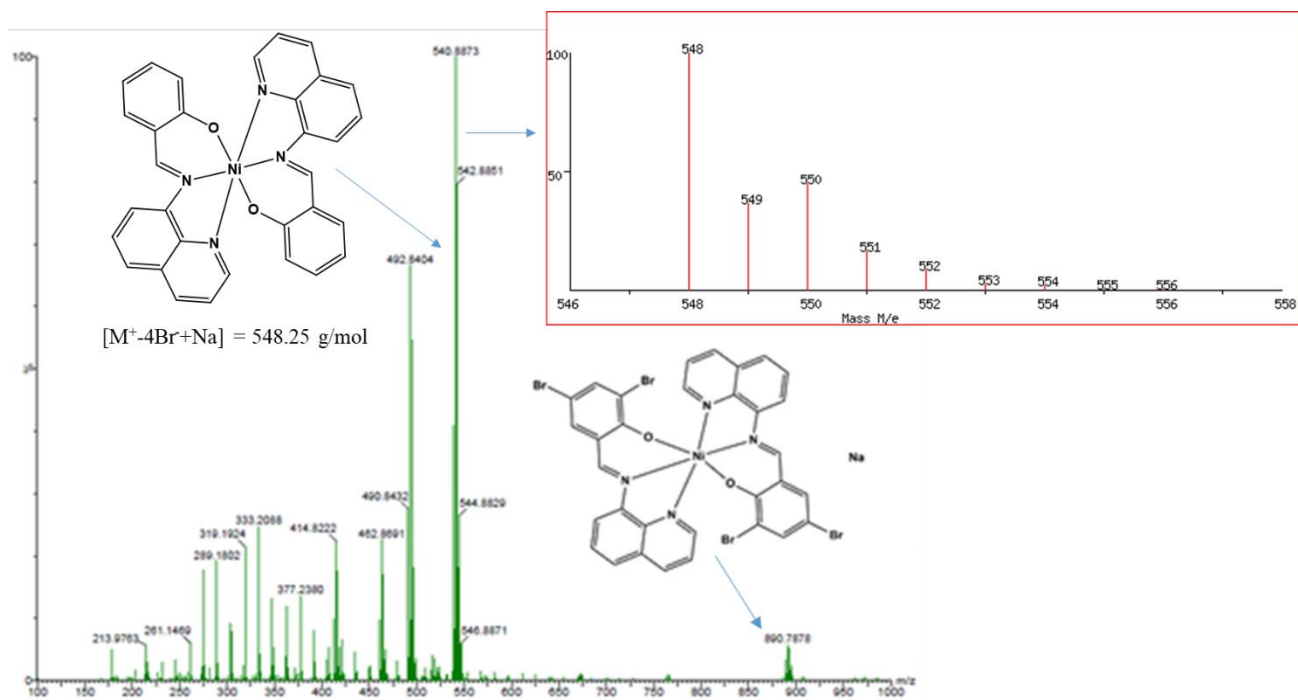


**Figure S30:** Mass spectrum of complex **Ni3**, showing the  $[Ni(L3)_2 + Na - 4Br^-]^+$  molecular ion peak at m/z of 890.7878 amu and the isotopic distribution of the molecular ion peak at m/z = 548 amu inserted.

***UV-vis studies of the late transition metal complexes***

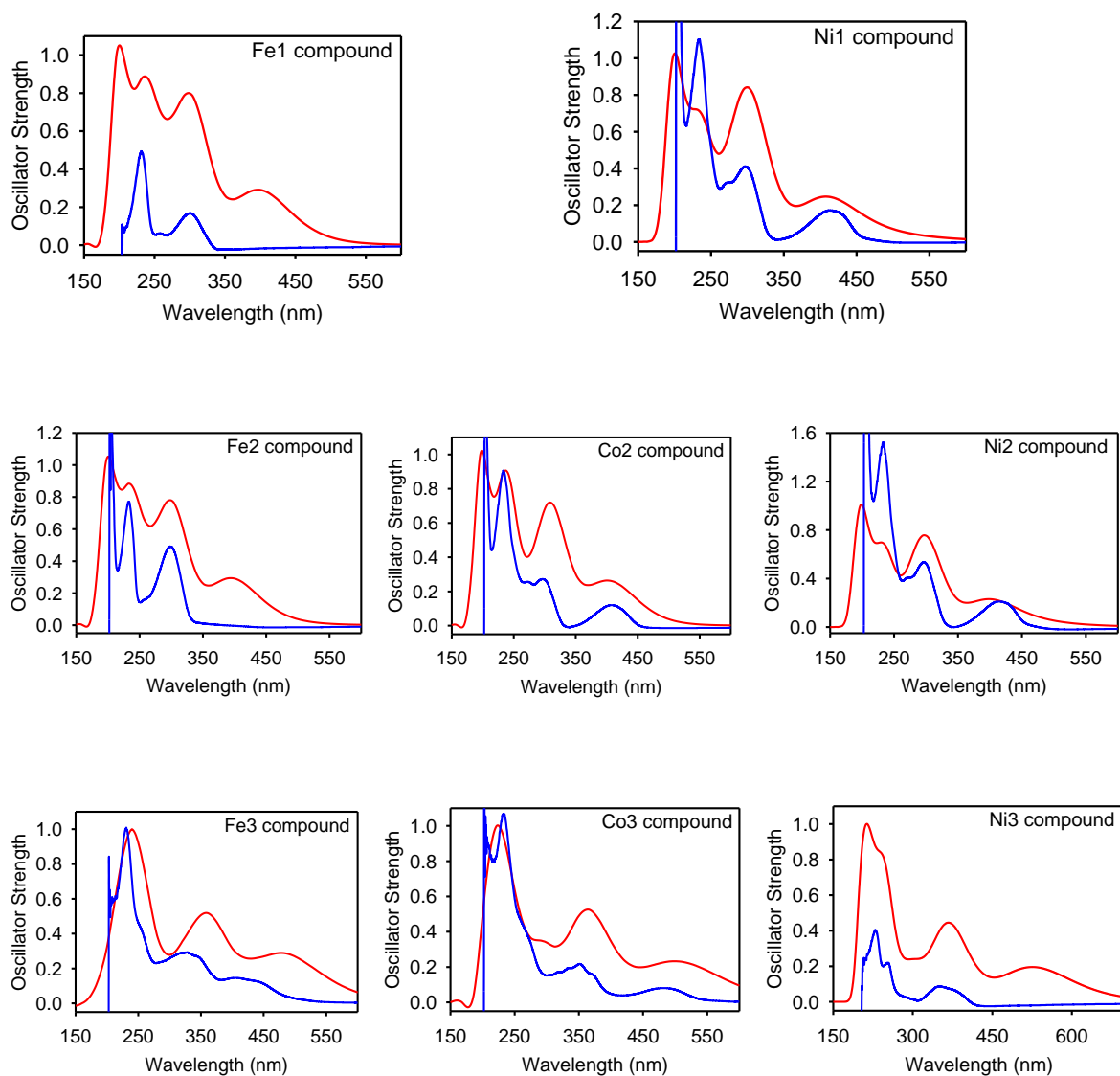


**Figure S31:** Absorption spectra of the metal complexes. The red curve shows the absorption spectra generated theoretically by using B3LYP functional whereas the black curve shows the absorption spectra generated experimentally.

## Ethylene oligomerization reactions

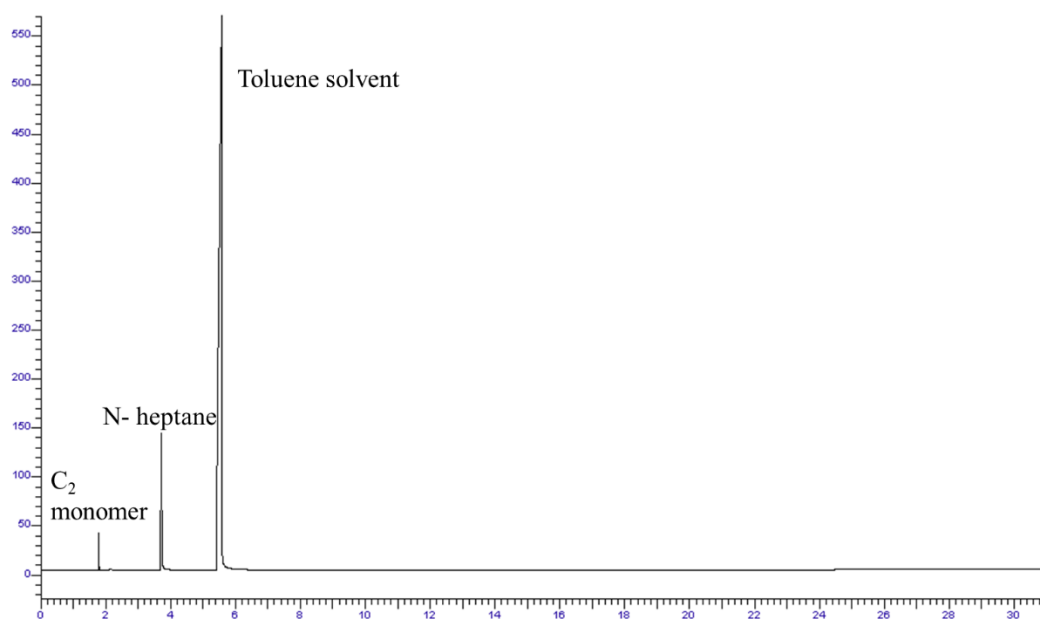


**Figure S32:** The GC-FID chromatogram showing no activity or formation of products when the Ni(II) complex **Ni1** is activated with MMAO-12 co-catalyst/toluene and used to catalyze the oligomerization of ethylene monomer in toluene solvent (Table 2, entry 10).

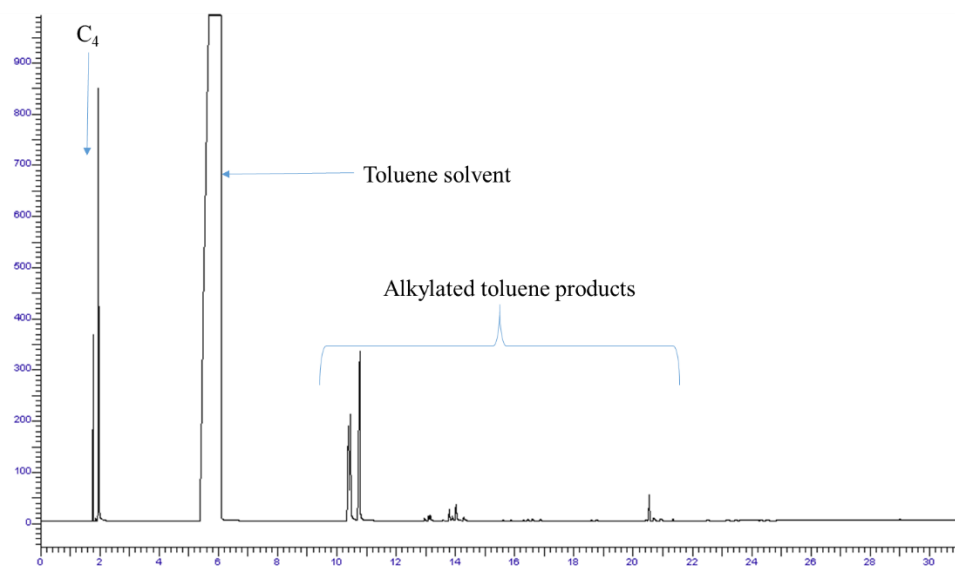


**Figure S33:** The GC-FID chromatogram showing the formation of C<sub>4</sub> oligomers and alkylated toluene products when the Ni(II) complex **Ni1** is activated by EtAlCl<sub>2</sub> co-catalyst/toluene and used to catalyse the oligomerization of ethylene monomer in toluene solvent (Table 2, entry 11).

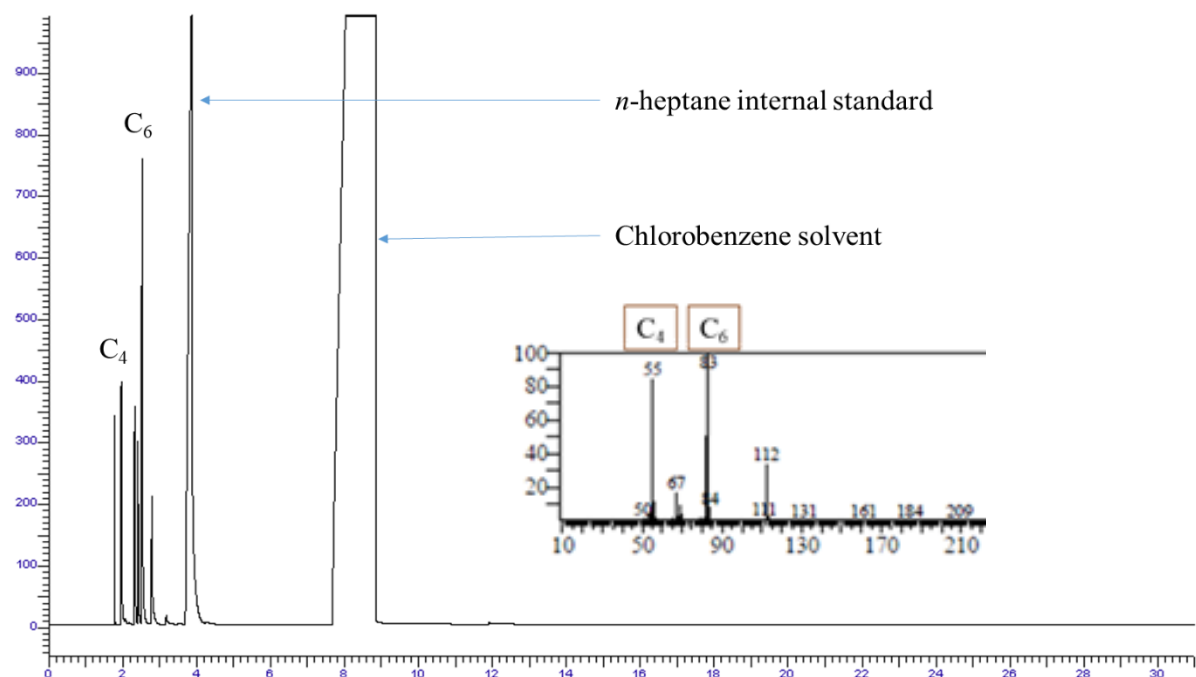


**Figure S34:** The GC-FID chromatogram showing the C<sub>4</sub> and C<sub>6</sub> oligomers obtained from **Fe1**/EtAlCl<sub>2</sub> system in chlorobenzene solvent (Table 2, entry 1). **Inset:** The GC-MS showing the molar masses C<sub>4</sub> and C<sub>6</sub> at 55 and 83 respectively.

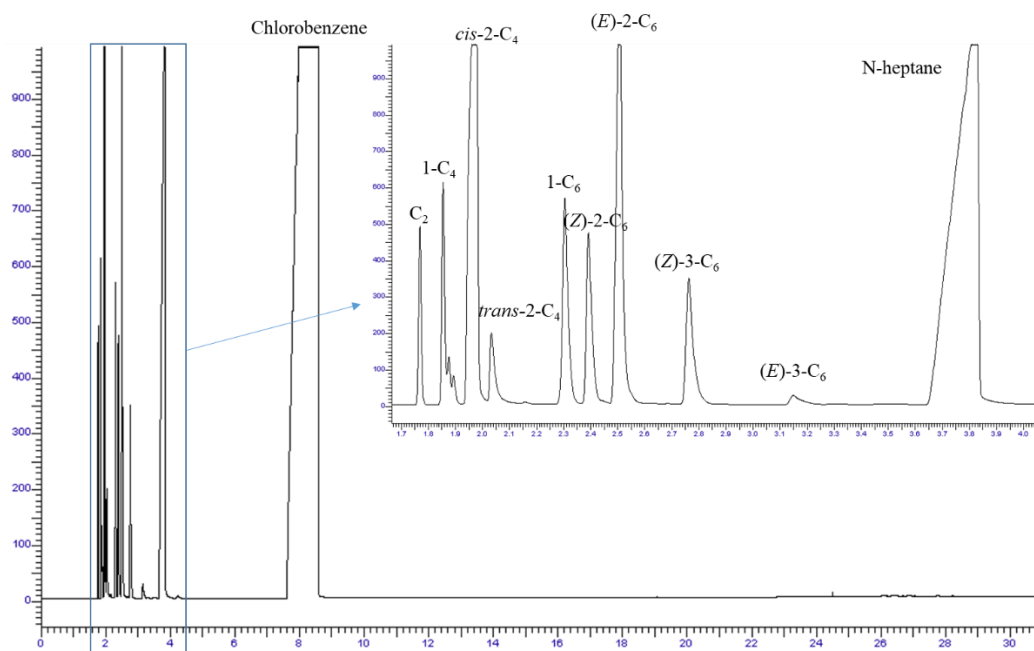


**Figure S35:** The GC-FID of **Ni1**/EtAlCl<sub>2</sub> system showing temperature effect on product distribution (Table 3, entry 10; T= 50 °C). Drastic drop in the composition of C<sub>4</sub> oligomer fractions from 60 % to 49 % was recorded.

*Density functional theory studies of the complexes*

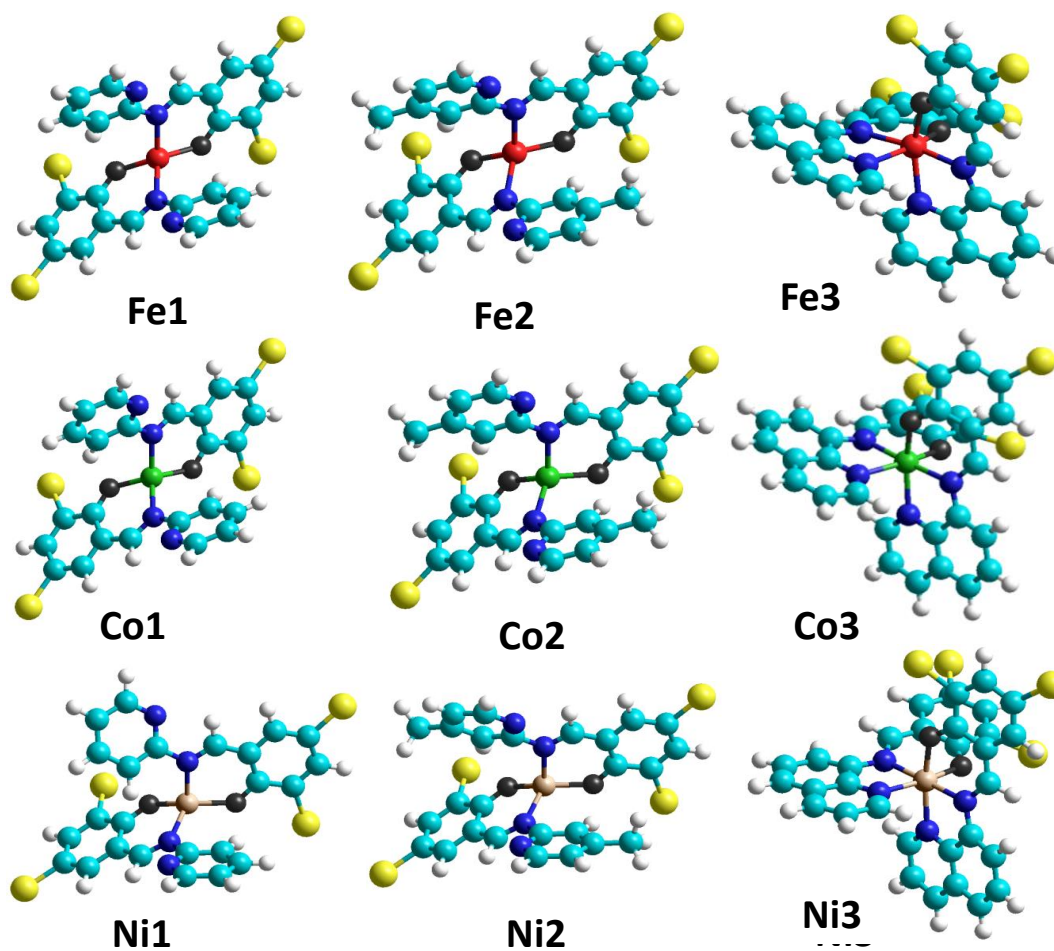


**Figure S36:** B3LYP optimized geometries of the metal complexes using Lan12dz basis set for metal cation and 6-311G(dp) basis set for the remaining atoms.

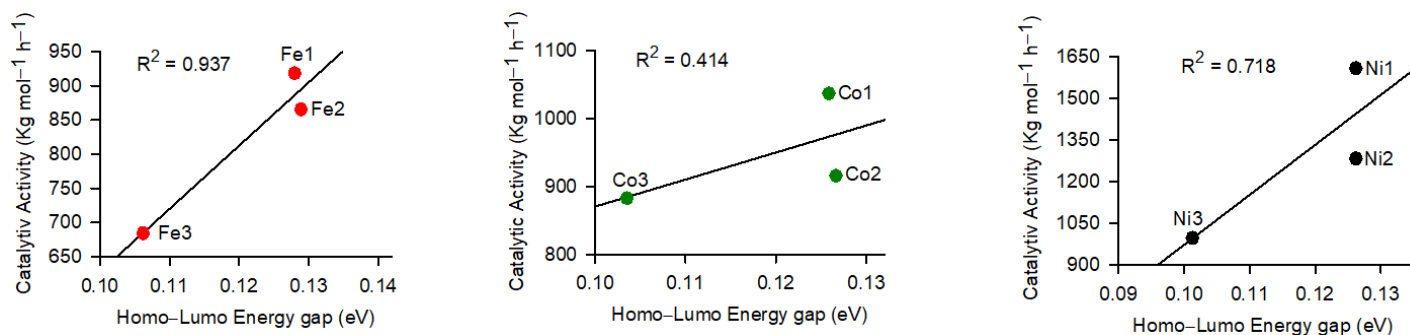


**Figure S37:** Dependence of catalytic activities in ethylene oligomerization of the metal complexes on their frontier orbitals.

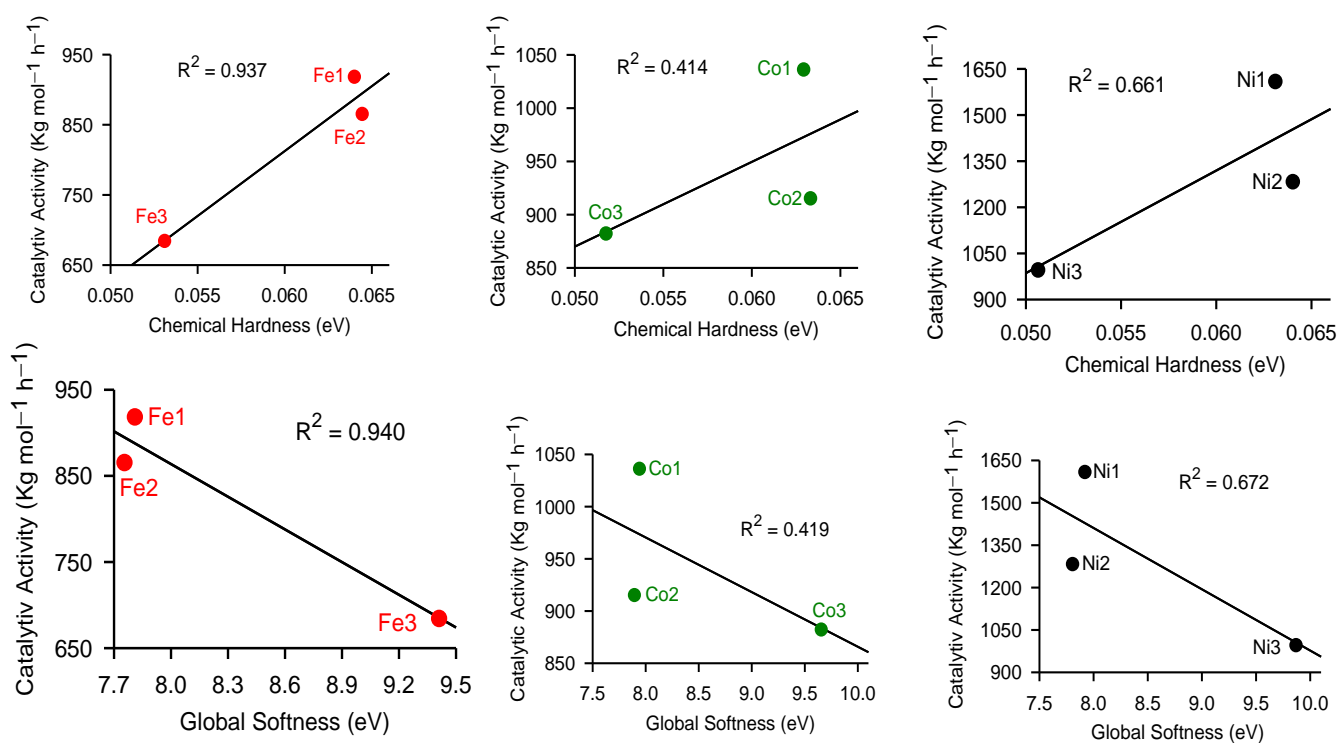


**Figure S38:** Dependence of catalytic activities in ethylene oligomerization on the global softness and chemical hardness of the metal complexes.

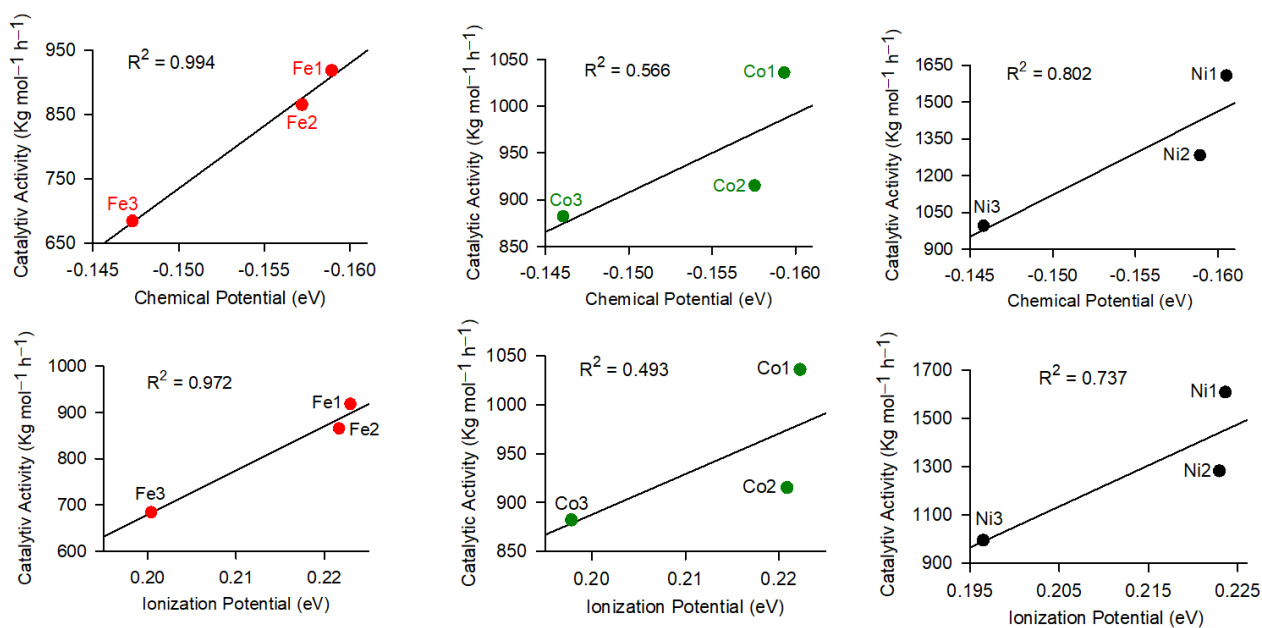


**Figure S39:** Dependence of catalytic activities on chemical and ionization potentials of the metal complexes. The more negative complexes were more activity, consistent with enhanced stability.

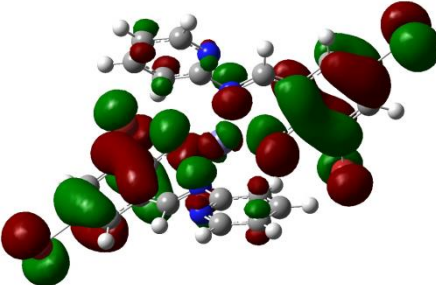
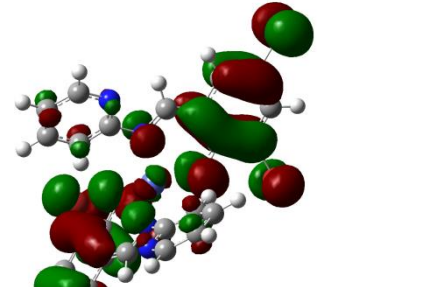
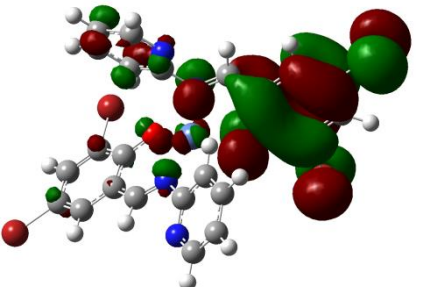
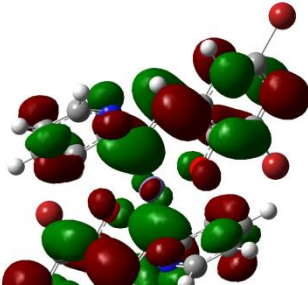
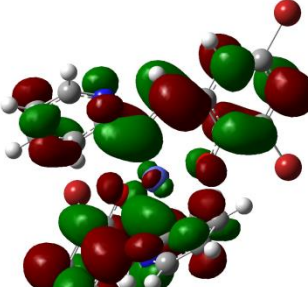
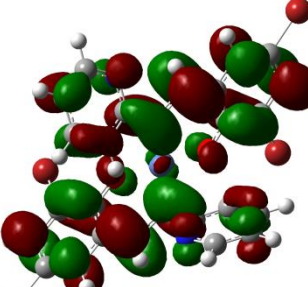
**Table S1:** X-ray crystallographic data and structure refinement for the **Fe3a** and **Ni3** complexes.

<b>Compound</b>	<b>Fe3a</b>	<b>Ni3</b>
Formula	C <sub>32</sub> H <sub>18</sub> Br <sub>4</sub> ClFeN <sub>4</sub> O <sub>2</sub>	C <sub>32</sub> H <sub>18</sub> Br <sub>4</sub> N <sub>4</sub> NiO <sub>2</sub>
<i>D</i> <sub>calc.</sub> / g cm <sup>-3</sup>	1.630	1.981
$\mu$ /mm <sup>-1</sup>	4.867	6.193
Formula Weight	901.44	868.85
Colour	orange	green
Shape	block	rod
Size/mm <sup>3</sup>	0.23×0.15×0.11	0.31×0.22×0.14
<i>T</i> /K	100(2)	100(2)
Crystal System	monoclinic	monoclinic
Space Group	<i>C</i> 2/ <i>c</i>	<i>P</i> 2 <sub>1</sub> / <i>c</i>
<i>a</i> /Å	33.700(4)	21.712(4)
<i>b</i> /Å	9.2687(11)	10.1595(17)
<i>c</i> /Å	24.484(3)	13.621(2)
$\alpha$ /°	90	90
$\beta$ /°	106.157(2)	104.217(8)
$\gamma$ /°	90	90
<i>V</i> /Å <sup>3</sup>	7345.6(16)	2912.5(8)
<i>Z</i>	8	4
<i>Z</i> '	1	1
Wavelength/Å	0.71073	0.71073
Radiation type	MoK <sub><math>\alpha</math></sub>	MoK <sub><math>\alpha</math></sub>
$\theta_{min}$ /°	1.258	1.935
$\theta_{max}$ /°	27.495	25.998
Measured Refl.	60212	30407
Independent Refl.	8417	5655
Reflections Used	6346	4594
<i>R</i> <sub>int</sub>	0.0556	0.0631
Parameters	461	401
Restraints	200	25
Largest Peak	3.076	4.520
Deepest Hole	-1.224	-1.323
GooF	1.069	1.140
<i>wR</i> <sub>2</sub> (all data)	0.1498	0.1792
<i>wR</i> <sub>2</sub>	0.1412	0.1728
<i>R</i> <sub>1</sub> (all data)	0.0788	0.0955
<i>R</i> <sub>1</sub>	0.0572	0.0787

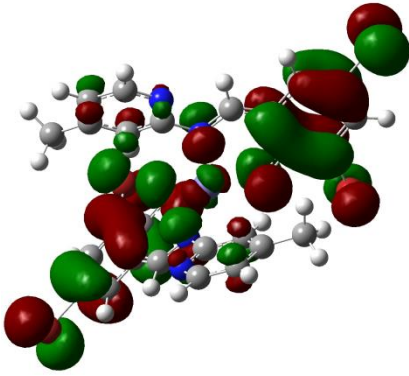
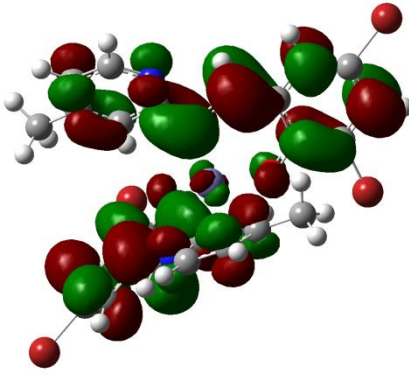
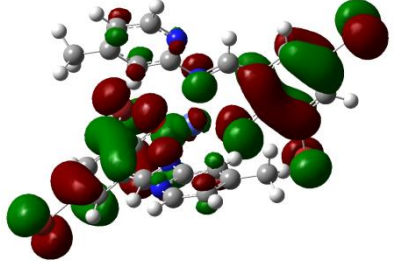
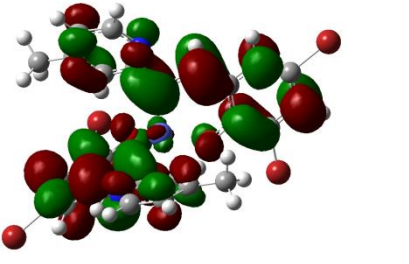
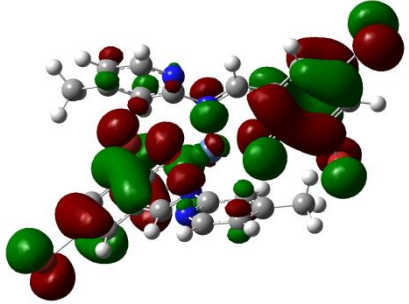
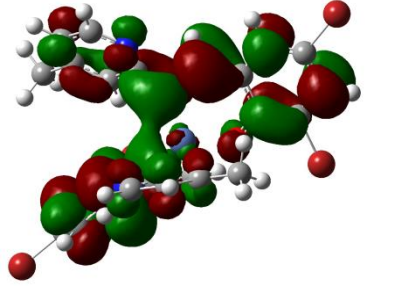
**Table S2:** Theoretical and experimental electronic transitions, oscillator strengths and assignments for metal compounds.

<b>B3LYP/6-311G(d,p)</b>					
<b>Metal Compound</b>				<b>Experimental</b>	
	$\lambda$ (nm)	$f$	$E$ (eV)	$\lambda$ (nm)	<b>Assignments</b>
<b>Fe2</b>	390	0.1025	3.1798	294	$d \rightarrow d$
	302	0.2319	4.0988	257	$n \rightarrow \pi^*$
	234	0.0747	5.2897	232	$\pi \rightarrow \pi^*$
	197	0.0804	6.2926	204	$n \rightarrow \sigma^*$
<b>Co2</b>	403	0.1123	3.0792	407	$d \rightarrow d$
	310	0.4242	4.0008	295	$n \rightarrow \pi^*$
	242	0.1523	5.1237	272	$\pi \rightarrow \pi^*$
	198	0.1337	6.2715	234	$n \rightarrow \sigma^*$
<b>Ni2</b>	402	0.0794	3.0874	414	$d \rightarrow d$
	308	0.2743	4.0254	296	$n \rightarrow \pi^*$
	236	0.1940	5.2622	274	$\pi \rightarrow \pi^*$
	200	0.1070	6.1924	233	$n \rightarrow \sigma^*$
<b>Fe3</b>	474	0.1287	2.6176	347	$d \rightarrow d$
	358	0.2238	3.4629	256	$n \rightarrow \pi^*$
	250	0.0985	4.9664	231	$\pi \rightarrow \pi^*$
<b>Co3</b>	503	0.1260	2.4660	–	$d \rightarrow d$
	361	0.2107	3.4359	353	$n \rightarrow \pi^*$
	305	0.0463	4.0713	271	$\pi \rightarrow \pi^*$
	239	0.0775	5.1789	233	$n \rightarrow \sigma^*$
<b>Ni3</b>	527	0.1329	2.3507	–	$d \rightarrow d$
	364	0.2520	3.3955	354	$n \rightarrow \pi^*$
	306	0.0516	4.0548	291	$\pi \rightarrow \pi^*$
	251	0.2574	4.9398	254	$\pi \rightarrow \pi^*$
	222	0.1510	5.5750	229	$n \rightarrow \sigma^*$

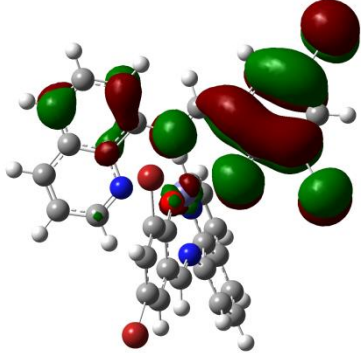
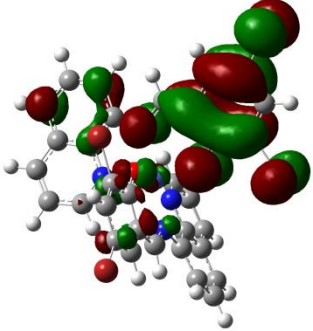
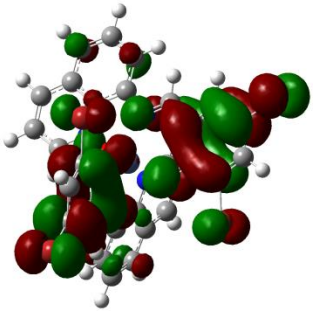
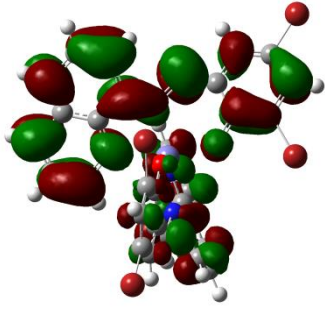
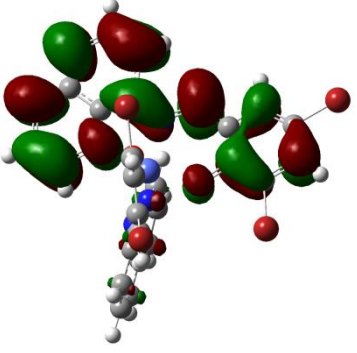
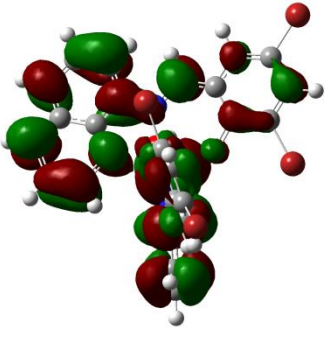
**Table S3.** The optimized DFT HOMO and LUMO frontier molecular orbitals of the **Fe1**, **Co1**, and **Ni1** metal complexes.

Metal Complex	HOMO Map	LUMO Map
<b>Fe1</b>	 The HOMO orbital map for the Fe1 complex shows a complex arrangement of red and green lobes. The red lobes are primarily located on the right side of the molecule, while green lobes are distributed across the left and central regions. The molecule is shown in a ball-and-stick model with white, red, and blue atoms.	
<b>Co1</b>	 The HOMO orbital map for the Co1 complex features a similar pattern of red and green lobes to Fe1. The red lobes are concentrated on the right, and green lobes are on the left. The overall structure is more compact than Fe1.	
<b>Ni1</b>	 The HOMO orbital map for the Ni1 complex shows a distribution of red and green lobes. The red lobes are on the right, and green lobes are on the left. The molecule has a more elongated and complex structure compared to Fe1 and Co1.	
	 The LUMO orbital map for the Fe1 complex shows a different distribution of red and green lobes. The red lobes are more prominent on the right side, and green lobes are on the left. The overall shape is similar to the HOMO map.	
	 The LUMO orbital map for the Co1 complex shows a distribution of red and green lobes. The red lobes are on the right, and green lobes are on the left. The structure is similar to the HOMO map.	
	 The LUMO orbital map for the Ni1 complex shows a distribution of red and green lobes. The red lobes are on the right, and green lobes are on the left. The structure is similar to the HOMO map.	

**Table S3.** The optimized DFT HOMO and LUMO frontier molecular orbitals of the **Fe2**, **Co2**, and **Ni2** metal complexes (*continued*).

Metal Complex	HOMO Map	LUMO Map
Fe2		
Co2		
Ni2		

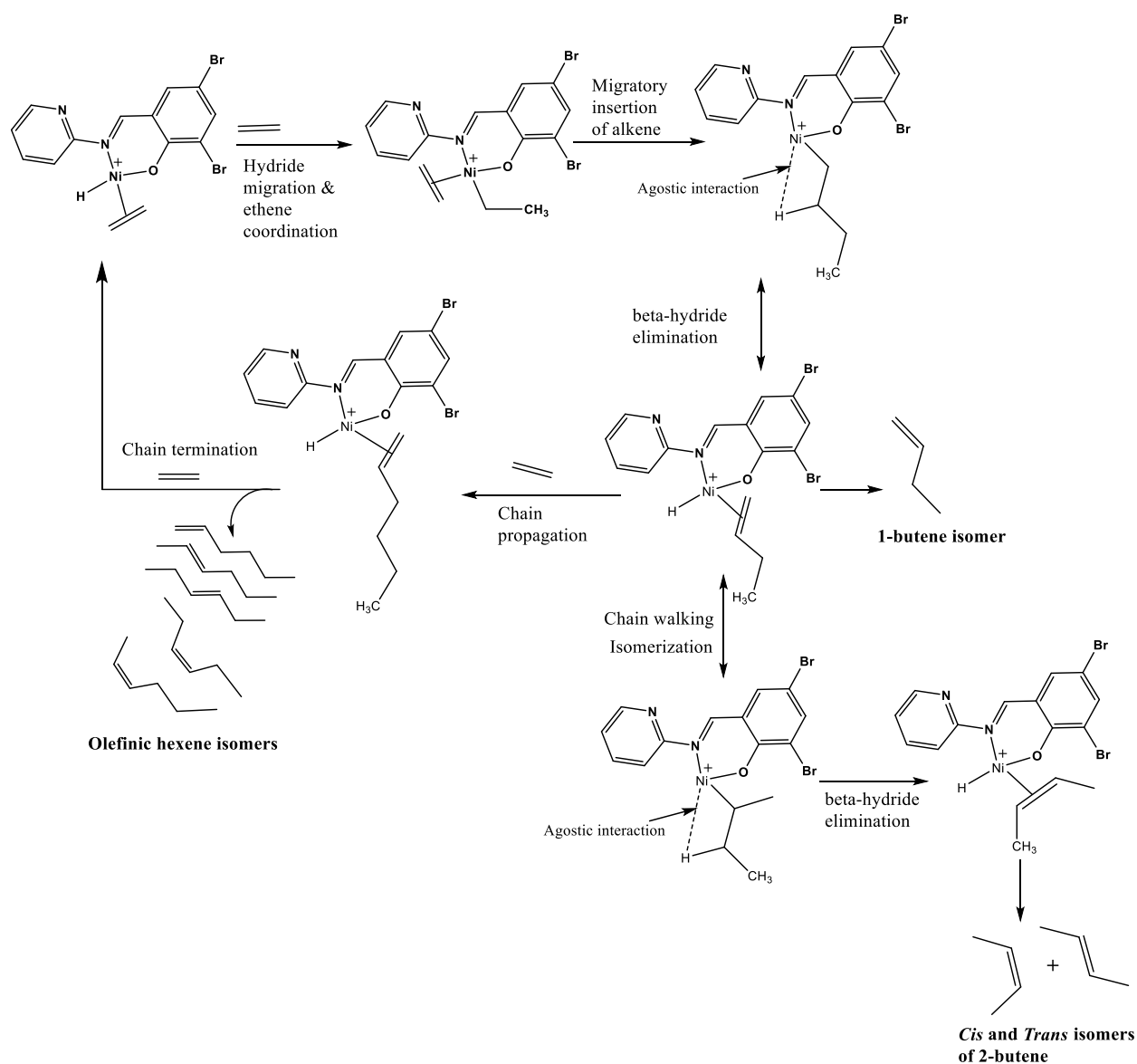
**Table S3.** The optimized DFT HOMO and LUMO frontier molecular orbitals of the **Fe3**, **Co3**, and **Ni3** metal complexes (*continued*).

Metal Complex	HOMO Map	LUMO Map
<b>Fe3</b>	 The HOMO orbital map for the Fe3 complex shows a complex arrangement of red and green lobes. The red lobes are primarily located on the right side of the molecule, while green lobes are distributed across the left and central regions. The molecule is shown in a ball-and-stick model with white, red, and blue atoms.	
<b>Co3</b>	 The HOMO orbital map for the Co3 complex features a central cluster of red and green lobes. The red lobes are more prominent and concentrated in the center, with green lobes extending outwards. The ball-and-stick model shows a similar structure to the Fe3 complex.	
<b>Ni3</b>	 The HOMO orbital map for the Ni3 complex displays a dense distribution of red and green lobes. The red lobes are concentrated in the lower and central parts of the molecule, while green lobes are more widespread. The ball-and-stick model shows a complex, multi-ring structure.	
		 The LUMO orbital map for the Fe3 complex shows a distribution of red and green lobes that is more spread out than the HOMO. Red lobes are visible on the left and right sides, with green lobes in the center. The ball-and-stick model is consistent with the HOMO map.
		 The LUMO orbital map for the Co3 complex shows a similar pattern to the HOMO, with red lobes being more prominent. The lobes are distributed across the central and peripheral regions of the molecule. The ball-and-stick model is consistent with the HOMO map.
		 The LUMO orbital map for the Ni3 complex shows a complex distribution of red and green lobes. Red lobes are concentrated in the lower and central parts, while green lobes are more widespread. The ball-and-stick model is consistent with the HOMO map.

**Table S4:** Optimization of the reaction conditions in ethylene oligomerization reactions using Ni1/EtAlCl<sub>2</sub> system.

Entry	Al/M	Time (h)	Pressure	Yield (g) <sup>b</sup>	Activity (kg mol <sup>-1</sup> h <sup>-1</sup> )	Product Distribution	
						(%) <sup>c</sup>	
						C <sub>4</sub> ( $\alpha$ -C <sub>4</sub> )	C <sub>6</sub> ( $\alpha$ -C <sub>6</sub> )
1	<b>100</b>	1	10	2.23	223	40 (98)	60 (19)
2	<b>150</b>	1	10	4.59	459	46 (95)	54 (18)
3	<b>200</b>	1	10	8.66	866	54 (92)	46 (15)
4	<b>250</b>	1	10	16.08	1608	60 (95)	40 (17)
5	<b>300</b>	1	10	4.18	418	35 (97)	65 (13)
6	<b>250</b>	0.5	10	6.09	1218	75 (98)	25 (31)
7	<b>250</b>	2	10	18.50	925	52 (88)	48 (13)
8	<b>250</b>	1	5	15.50	1550	55 (92)	45 (17)
9	<b>250</b>	1	20	10.25	1025	46 (92)	54 (20)
10 <sup>d</sup>	<b>250</b>	1	10	9.96	996	49 (79)	51 (11)
11 <sup>e</sup>	<b>250</b>	1	10	6.60	660	52 (64)	48 (9)

<sup>a</sup>Reaction conditions: complex, 10  $\mu$ mol; solvent, chlorobenzene, 30 mL; temperature, 30 °C; time, 1 h; pressure, 10 bar; EtAlCl<sub>2</sub>: Al/M=200; <sup>b</sup>Determined using GC and n-heptane served as an internal standard. <sup>c</sup>Determined by GC and GC-MS. <sup>d</sup>T=50 °C, <sup>e</sup>T=70 °C. The optimized conditions were obtained as temperature, 30 °C, time, 1 h, Al/Ni, 250 and pressure of 10 bar (entry 4).



**Scheme S1:** The proposed mechanism for the formation of 1-butene, *cis* and *trans* isomers of 2-butene and the favoured production of internal hexene oligomers by the Fe(II), Co(II) and Ni(II) complexes. The absence of C<sub>8</sub> oligomers implies that after the formation of C<sub>6</sub> oligomer, chain isomerism and termination was more favoured than chain propagation to form long chain C<sub>8+</sub> oligomers.